Multi-spectral investigation of ozone: Part I. Setup & uncertainty budget

Christof Janssen, Corinne Boursier, Hadj Elandaloussi, Pascal Jeseck, Dmitry Koshelev, Patrick Marie-Jeanne, Christian Rouillé, David Jacquemart, Florence Thibout, Mélanie Vaudescal-Escudier, et al.

Multi-spectral investigation of ozone: Part I. Setup & uncertainty budget

Christof Janssen[a,*], Corinne Boursier[a], Hadj Elandaloussi[a], Pascal Jeseck[a], Dmitry Koshelev[a,1], Patrick Marie-Jeanne[a], Christian Rouillé[a], David Jacquemart[b], Florence Thibout[c], Mélanie Vaudescal-Escudier[d,2], Yao Té[a]

[a]*Sorbonne Université, Observatoire de Paris, Université PSL, CNRS, Laboratoire d'Etudes du Rayonnement et de la Matière en Astrophysique et Atmosphères, LERMA-IPSL, 75005 Paris, France*
[b]*Sorbonne Université, CNRS, De la MOlécule aux NAno-objets : Réactivité, Interactions et Spectroscopies, MONARIS, 75005 Paris, France*
[c]*Laboratoire Kastler Brossel, Sorbonne Université, CNRS, ENS-Université PSL, Collège de France, 75005 Paris, France*
[d]*Sorbonne Université, CNRS, Institut des NanoSciences de Paris, UMR7588, 75252, Paris, France*

Abstract

This is the first in a series of two papers concerned with new accurate high resolution spectroscopic measurements of line positions and intensities of ozone in the 5 µm and 10 µm regions using a commercial Michelson Fourier transform spectrometer. Measurements in both wavelength regions have been made quasi simultaneously using a special H-shaped absorption cell with two parallel absorption paths of different length that remained connected during the experiments. Accurate ozone partial pressures were monitored on the shorter of the two paths using UV absorption at the 253.65 nm Hg reference line. In this paper, we report in detail on the experimental setup and provide a comprehensive uncertainty analysis. The spectral analysis and retrieved line parameters are provided in the second paper, which also contains the comparison to the literature data. Line positions have been measured with standard uncertainties of $u(\nu_0) = 3 \cdot 10^{-5}\,\mathrm{cm}^{-1}$ in both spectral regions, mainly in the ν_3 and the $\nu_1 + \nu_3$ bands of ozone. Intensities of most of the transitions in the ν_3 band have a relative standard uncertainty of $u_r(S) = 1.1 \cdot 10^{-2}$. The uncertainty is slightly smaller for intensities in the $\nu_1 + \nu_3$ band at 5 µm. The highly accurate experimental data provide a benchmark for molecular calculations and the 1.1% line intensity uncertainty will help resolving the discrepancy between UV and IR atmospheric ozone retrievals and correcting current biases in spectroscopic databases.

Keywords: ozone, atmospheric composition, remote sensing, FTIR, MIR, spectroscopic database

1. Introduction

Ozone (O_3) plays a key role in the Earth's atmosphere. It serves as a precursor for atmospheric radicals (such as NO_3 and OH), influences atmospheric oxidation, is a green-house gas, impacts the thermal structure of the middle atmosphere and provides a unique UV shield for Earth's biosphere. It is thus a key molecule in the Earth system and its observation is given particular attention in global watch programs dedicated to the monitoring and understanding of climate and atmospheric composition change [1].

Absolute ozone absorption cross sections and intensities have been a long-standing issue in atmospheric remote sensing and gas metrology [2–4]. In the 2004 update of the HITRAN database, the results of three then highly consistent and recent spectroscopic investigations [5–7] were used to redetermine recommended intensities in the ozone fundamental bands. They were preferred over the outcome of another study of that time [8] that had about 4% higher average intensities in the ν_1 and ν_3 fundamental bands around 10 µm. Ever since, questions on the claimed data base accuracy of about 1% and the appropriateness of the correction have been raised. Both, laboratory [9, 10] and atmospheric measurements [11, 12] that simultaneously compared ozone concentrations using UV and IR spectroscopic data, found that the previous HITRAN database version was more compatible with recommended UV data.

Despite recent experimental and theoretical improvements, the issue is only now about being resolved: Guinet et al. [13] have investigated 15 strong ozone

*corresponding author
Email address: christof.janssen@upmc.fr ()
[1]now at Criteo, 32 rue Blanche, 75009 Paris, France
[2]now at CNRS, Univ. Bordeaux, PLACAMAT, UMS 3626, 33600 Pessac, France

lines in a narrow region around 1133 cm^{-1} using tunable diode laser spectroscopy and found that HITRAN intensities are lower by about 2.5%. The observed dispersion of the measurements was 0.8% and ozone partial pressures have been obtained from Hg lamp photometry using the UV absorption cross section value of the University of Minnesota group [4]. At the same time, Thomas et al. [14] remeasured ozone intensities both in the 5 μm and 10 μm bands with a high resolution FTIR instrument, which essentially confirm the new HITRAN data. On average, the intensities of 65 strong transitions in the 10 μm region differed by only −0.3% from the HITRAN values, with individual intensity ratios showing a scatter of 0.9%. However, the observed discrepancy at 5 μm seems significant. In this range 18 well suited transitions had line strengths lower than HITRAN by 2.0% on average, with the scatter of individual measurements being 1.2%. More recently, Janssen et al. [15] performed atmospheric column measurements of ozone to compare intensities in the $\nu_1 + \nu_3$ band at 5 μm with line strengths at 10 μm using the high resolution FTS-Paris instrument. Depending on the transitions, lines accessible to atmospheric observations at 5 μm are either 1% to 1.5% too low (P-branch of the $\nu_1 + \nu_3$ band) or about 1% too high (P, Q, and R-branches) when compared to intensities at 10 μm. Since the majority of intensities at 5 μm were lower as compared to the data around 10 μm, this atmospheric measurement seems to be in line with the observation of Thomas et al. [14] who also found that HITRAN intensities around 5 μm are too low when compared to intensities at 10 μm. Shortly after, Drouin et al. [16] have used THz spectroscopy to determine ozone partial pressures for measuring IR intensities of 767 transitions in the 10 μm range. After a very recent reanalysis [17], these data indicate the necessity of correcting HITRAN 2016 fundamental intensities at 10 μm by ∼ +3.3%, but the single measurement dispersion of 2.8%, and the relative uncertainty of the ozone mole fraction determination of 1.5% [16], still do not warrant correction of database values.

Very recently, the UV absorption cross section at the 253.65 nm Hg line position, frequently used as a reference for determining ozone partial pressures in cross section or line intensity measurements, has been critically reevaluated based on a literature review [18]. It confirms that the reference value of Hearn [19] and UV cross sections based thereon are biased by about 1.25%. This applies directly to atmospheric retrievals based on cross sections from Bass and Paur [20, 21] that were referenced to Hearn's value, but it does not affect more recent UV cross section measurements [22, 23] that seem well compatible with the lower absorption cross section value. Therefore, and also because observed UV-IR discrepancies are usually based on UV cross sections in the Huggins bands ($\lambda > 300$ nm), this reevaluation has no immediate impact on identifying biases of IR data from direct UV-IR inter-comparisons. The recent redetermination of the ozone absorption cross section at the 325 nm HeCd laser line, however, implies that currently recommended [24] UV cross sections of Gorshelev et al. [22] or Malicet et al. [23] might suffer from a ∼ +2% bias. This has recently been corroborated in a temperature dependent FTS study [25], which reports an even 0.5% lower cross section under the same conditions (λ = 325.126 nm (vacuum) and T = 294.1 K). Given that comparisons with the 10 μm bands [9–11] led to discrepancies between 4% and 5%, this implies that the 10 μm intensities in HITRAN are biased by 2% to 3% towards lower values and that a corresponding augmentation of the database intensities is necessary to remove the bias.

While there is thus ample evidence that IR intensities in databases such as HITRAN 2016 needed to be increased by a few percent, previous results were too indirect, too ambiguous and not accurate enough to yet justify quantitative correction ~~of the present data~~. This demonstrated the urgent need for more accurate spectroscopic data which are consistent over different spectral regions. Moreover, a full uncertainty budget is desirable to assess the significance of a potential bias correction. Based on requirements in atmospheric research and air quality control [24] an uncertainty level of better than 1% should be realized, knowing that intensities are not the only factors limiting the accuracy of atmospheric remote sensing in the IR which requires other spectroscopic parameters such as pressure broadening and shifting coefficients to be well specified too [15, 26, 27]. Corresponding investigations have been carried out by several research groups and some of these very recent results are published as part of the current special issue. An evaluation of new measurements in the 10 μm region has been made at DLR in Oberpfaffenhofen [17]. GSMA at Reims have recently remeasured ozone at 5 μm and 10 μm [28] leading to an update (2020d) of the S&MPO database [29, 30]. Both, the new Reims and the Oberpfaffenhofen data are published in the public domain [31]. The present paper is the first in a series of two where a detailed account of new quasi simultaneous measurements in the 5 μm and 10 μm domains using a high resolution FTS are given. A preliminary evaluation of our measurements has already been compared to ab initio calculations [28]. Here in paper I, we describe the new experimental setup that allows for quasi simultaneous measurements of intensities in the 5 μm

and 10 μm regions and thus assures a high level of consistency between the two wavelength ranges. Continuous UV absorption measurements at the 253.65 nm Hg line wavelength allow for accurate determination of the ozone partial pressure during the measurements. Using the recently recommended cross section value [18] further ensures that our mid-IR measurements agree with this standard. Based on the experimental conditions we also present a detailed uncertainty budget that follows standard procedures outlined by GUM [32]. The measured line parameters and the comparison to literature data and databases, including the new [33] and earlier versions of HITRAN, will be presented in Paper II of the series [34].

2. Experimental

The optical arrangement is shown in Fig. 1. A special H shaped absorption cell is made from two parallel Pyrex tubes at 250 mm distance and with 50 mm and 30 mm diameter and 50 mm and 200 mm length, respectively. While the long tube ends are sealed with wedged KBr windows, the short tube is equipped with wedged BaF_2 windows. All windows were glued using a UV curing epoxy.

The cell is integrated in the sample compartment of a Bruker HR FTS instrument, which is described in the next section (2.1). It can be simultaneously traversed by one UV and either of two IR light paths (see panels a and b of Fig. 1).

2.1. FTS

Spectra were taken using the IFS 125HR (Bruker) Fourier transform (FT) spectrometer of the FTS-Paris station, which is part of the international TCCON network [35]. During regular operation the FTS is coupled to a sun tracker, but the instrument can also be used for laboratory investigations using an integrated globar as light source. The Michelson interferometer system that has been employed with a KBr beam splitter has a maximum optical path difference of 257 cm, corresponding to an unapodized spectral resolution of $2.35 \cdot 10^{-3}$ cm^{-1} (FWHM). Two different light paths can be selected: one that employs a MCT detector and one that impinges on an InSb detector, with appropriate optical filters to either cover the 10 μm or the 5 μm spectral range. A detailed description of the instrument that is operated in vacuum (residual pressure < 2 Pa) can be found elsewhere [36]. The measurement configuration is presented in Table 1. The wavenumber stability of the instrument has been explored in a long duration (∼ 20 h) acquisition of N_2O spectra during the measurement period. The Allan-Werle analysis of the derived line positions, exemplified by the P1e transition of the ν_3-band, demonstrates a stability of better than $5 \cdot 10^{-6}$ cm^{-1} over the maximum acquisition period of 13 h in this investigation (Fig. 2).

Table 1: Configuration of the FTS-Paris for the 5 μm and 10 μm ozone measurements.

Parameter	MCT channel	InSb channel
Wavelength region (μm)	10	5
Spectral range (cm^{-1})	750 – 1300	1900 – 3100
Field stop aperture (mm)	1.15	
Integration time (min)	14 (8 scans)	
Number of averaged spectra per sequence	8	4
Number of sequences	5	5
Number of averaged spectra	40	20

2.2. Sample preparation and cell filling

Ozone has been produced from high purity research grade oxygen (99.9995%, Air Liquide) by electric discharge in a glass reactor with external electrodes. The set-up was designed to limit the use of metallic surfaces and is similar to a system already described elsewhere [37]. Liquid nitrogen (LN_2) was utilized to condense ozone during the discharge and more than 50% (typical 0.5 mmol) of the initial oxygen was converted. The ozone was then separated from the oxygen by pumping on the gas phase for several minutes while keeping the LN_2 bath to hold back the condensed ozone. Thereafter, ozone was allowed to enter the gas phase and the required amount was transferred into a glass cold finger close to the inlet of the cell. The cold finger containing the condensed ozone was once again pumped to remove residual oxygen. The cell was then filled with the content of the cold finger, without measuring its quantity. Just before the cell filling, the 10 Torr pressure head had been filled with oxygen at the expected ozone pressure, such that pressure in the cell could be determined by briefly opening the cell and balancing pressure with the oxygen at the pressure gauge. Usually, a match within 20% of the target pressure could be obtained. After equilibration and pressure reading, the cell was closed as rapidly as possible to minimize ozone decomposition on the pressure head. The continuous UV measurements (see Section 2.3) provided in situ measurements of the ozone partial pressure, using cell length and absorption cross section values specified in Sections 3.2.1 and 3.3. The mole fractions of oxygen (O_2) at filling and during the recording of the IR spectra have been obtained from instantaneous ozone partial

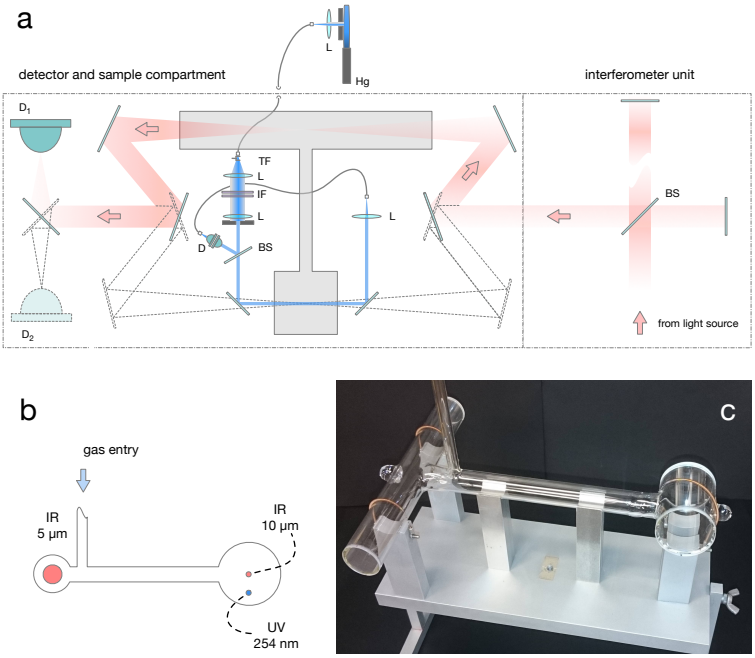

Figure 1: Illustration of the optical setup. Panel a provides a top view of the FTIR spectrometer with its principal optical components (strongly simplified optical arrangement) and the sample compartment with the integrated H-shape absorption cell. UV and IR light paths are indicated by blue and red color, respectively. The IR light path can be made to pass either arm of the cell and use either of two detectors (InSb (D_1) or MCT (D_2)), indicated by dashed light paths and elements. Abbreviations are as follows. Hg – low pressure Hg discharge lamp (pencil type), L – lens, BS – beamsplitter, TF – tuning fork, IF – interference filters, and D – Si photo diodes. Optical fibers are indicated by bent grey lines. The lower left panel b shows a head on view of the cell. It indicates that the UV light path crosses the short arm about 15 mm below the cell's central axis. Beam diameters on the cell windows are also shown. Panel c represents a photograph of the glass cell.

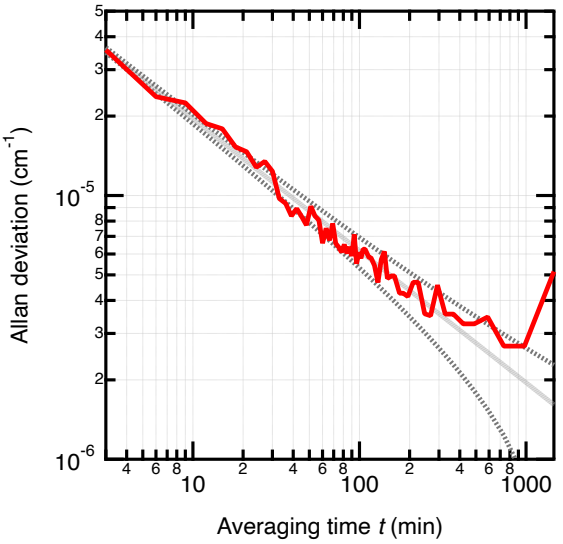

Figure 2: Allan-Werle plot of the N_2O line position at 2222.918750 cm^{-1} from cell spectra recordings using the FTS-Paris.

pressures, assuming that oxygen is the dominant residual gas during filling ($p_{tot} = p(O_3) + p(O_2)$) and that any ozone decomposition in the cell results in complete conversion into molecular oxygen ($3\Delta p(O_3) = -2\Delta p(O_2)$).

For our measurements, the absorption cell has been filled six times at roughly four different pressures between 0.15 Torr and 1.2 Torr (0.2 hPa and 1.5 hPa). During data acquisition of about 13 hours (see Section 2.3), slow decomposition (between 1% and 2%) of ozone has been observed using UV absorption. The linear decrease of the ozone concentration allowed to assign a well defined average ozone partial pressure as a function of the chosen acquisition intervals. These and corresponding averaged foreign gas contents are displayed in Table 2. Ozone decomposition rates vary between $-2.2 \cdot 10^{-7}$ s^{-1} and $-4.9 \cdot 10^{-7}$ s^{-1} and are largest at the lowest pressure. The characteristic ozone lifetime exceeds 23 days.

2.3. Data acquisition

While temperature and UV absorption measurements have already begun before the cell was filled using a multifunction DAQ card integrated into a PC, IR spectrometer measurements have been started thereafter utilizing the OPUS software package provided by the spectrometer maker. Spectra were acquired in an alternating sequence with recordings switching between the 5 µm and the 10 µm region. The integration time of 8 co-additions per channel is 14 min. 4 consecutive InSb measurements (56 min) or 8 MCT measurements (112 min) have been obtained before switching channels. The recording of one sequence covering both wavelength regions thus takes 168 minutes and altogether 5 full acquisition sequences have been performed. Data in the 5 µm region have therefore been acquired within about 12 h and those in the 10 µm region within ca. 13 h. Addition of all spectra obtained on the same path yielded signal to noise (peak to peak) ratios of about 120 at 10 µm and 350 at 5 µm. The corresponding acquisition parameters are summarized in Table 1.

3. Analysis and uncertainties

3.1. Wavenumber scale and line positions

The wavenumber scale has been calibrated in a set of additional experiments where the H-cell has been filled with pure nitrous oxide at low pressure ($\leq$ 1 hPa). Recently, N_2O line positions in the ν_1 and ν_3 fundamental bands at 4.5 µm and at 7.8 µm have been determined accurately by Ting et al. [38] and AlSaif et al. [39], respectively. The two bands are within either of the two spectral windows at 5 µm and at 10 µm that we have used. Taking the largest uncertainty in both of the studies, relative uncertainties are $1.4 \cdot 10^{-9}$ at 4.5 µm and $4.7 \cdot 10^{-9}$ at 7.8 µm. We also note that the N_2O line positions are in good agreement with wavenumber calibration data recommended by NIST [40] which has relative standard uncertainties of $3.6 \cdot 10^{-8}$ and $1.6 \cdot 10^{-8}$ for the fundamental transitions in the 7.8 µm and 4.5 µm regions, respectively.

The comparison with N_2O line positions in both ranges has allowed to calibrate the FTS instrument using a relative frequency shift parameter η between directly observed ozone line positions ν_{obs} and the unbiased line positions ν_0:

$$\nu_0 = \nu_{obs}\,(1+\eta)^{-1}\,. \qquad (1)$$

This definition corresponds to η being the relative difference between observed and "true" positions. For 4.5 µm, thus for the window covering the 5 µm ozone bands, we find $\eta = (4.95 \pm 0.02) \cdot 10^{-7}$ and for the 7.8 µm acquisition region including the ozone bands at 10 µm one obtains $\eta = (4.29 \pm 0.06) \cdot 10^{-7}$. Values reflect the uncertainty of the reference line positions as well as the statistical error of the mean of the 25 and 77 lines used for the fitting at 4.5 µm and 7.8 µm, respectively. η-values of several 10^{-7} are quite typical for a IFS 125HR instrument [41]. It is interesting to note that the two different η-values are almost identical when the effect of the instrumental line shape function is taken into account. Asymmetric apparatus functions lead to

Table 2: Measurement conditions.

No	Temperature (K)	Ozone pressure (Pa)		Foreign gas content (mmol/mol)		Ozone decomposition
		5 µm	10 µm	5 µm	10 µm	rate (10^{-7} s^{-1})
1	297.64	152.52	152.35	10	12	−2.2
2	297.79	86.89	86.74	40	42	−2.9
3	297.76	42.98	42.91	62	64	−3.0
4	298.38	19.05	19.00	130	134	−4.9
5	298.04	79.71	79.56	43	45	−3.7
6	298.68	155.76	155.46	40	42	−3.7

shifts in the observed positions [42], and the more positive value is consistent with the more asymmetric instrument line shape in the 5 µm region. The uncertainty of an individual position measurement, however, is dominated by the precision at which a single line position can be inferred in the spectral fitting process. We use the scatter of the determinations of the N_2O reference line positions around 1270 cm^{-1} to determine this uncertainty and find a relative standard deviation of $2.1 \cdot 10^{-8}$ from the 77 different line positions. The relative standard uncertainty of the line position determination can then be obtained by adding the uncertainty of the calibration (η). In absolute terms, the standard uncertainty is $u(\nu) = 3 \cdot 10^{-5}$ cm^{-1}. In the 5 µm range, the scatter of the observed positions of the reference lines was 7 times smaller, implying a roughly three to four times smaller absolute uncertainty. For reasons of simplicity, however, we stick with the more conservative standard uncertainty $u(\nu) = 3 \cdot 10^{-5}$ cm^{-1} for both regions.

Since the wavenumber calibration measurements have been undertaken with the same setup and same optical settings, but a few days after the ozone investigations, we have checked whether an instrumental drift occurred during that period. To this end, 18 selected transitions of CO_2 in the ν_3-band at 4.3 µm have been determined in both, the ozone and in the N_2O spectra. The same lines appeared in both types of spectra due to the presence of carbon dioxide traces in the residual spectrometer gas. According to this comparison, the frequency shift parameter (η) of the type of spectra differed only insignificantly (by $3 \cdot 10^{-9}$) and by much less than the wavenumber uncertainty. We have therefore assumed that the instrument remained stable between the measurements and the calibration.

3.2. Absorption length

The effective absorption lengths in the H-shaped cell have been determined carefully using a home-built laser interferometer [43]. The results of these measurements

Table 3: Interferometrically determined path lengths with standard uncertainties given in parentheses as last digits of the result. Effective IR path lengths due to the presence of multiple reflections are also indicated.

	long arm	short arm
inner window distance d / mm	200.024(48)	50.820(14)
IR path (geometric) / mm	200.357(66)	50.919(31)
IR path (effective) L_{IR} / mm	200.50(93)	51.06(34)
UV path L_{UV} / mm	–	50.961(72)

are shown in Table 3. They include geometric measurements detailed hereafter as well as multiple reflection effects which are evaluated in Section 3.2.3. The uncertainty of the interferometric length determination is dominated by the fringe number measurement on the one hand and by the determination of the refractivity of the gas used for the length measurements on the other hand. The latter depends on molecular constants as well as on temperature and pressure measurements. Since temperature gradients during the actual measurements were higher than those reported earlier [43], the relative standard uncertainties of 0.24 ‰ or 0.28 ‰ were elevated likewise, when compared to the 0.18 ‰ advertised in the original article. While the effect of the windows not being parallel can be neglected in our case [see Ref. 44, for a discussion], the effective absorption path lengths L (UV, IR) differ from the inner window distance d due to two reasons. First, UV and IR beams are slightly inclined with respect to the cell's central axis. Second, all beams show a slight divergence. If inclination angles and the divergence are small, the absorption path length L is simply given by

$$L = \frac{2}{3} d \left(\sec^3(\alpha_m) - 1 \right) \cot^2(\alpha_m) \sec(\theta), \qquad (2)$$

where θ is the inclination of the beam's central axis with respect to the optical axis of the cell and where α_m is the divergence angle. The $\sec(\theta)$ dependence describes the

prolongation of a collimated beam in an inclined cell with parallel windows. The dependence on the beam divergence in Eq. (2) is exact for $\theta = 0$, and assuming that the convergent beam is symmetric around the central axis and that the radial intensity dependence is due to a collimated homogeneous beam being focalized. For small θ, Eq. (2) is a very good approximation, as the error made is only on the order of $\alpha_m^2\theta^2$. For our beam configurations, this contribution never exceeds 1 part in 10^5 (see Appendix). The uncertainty of the effective path length determination is obtained following standard propagation rules, which lead to

$$u_r^2(L) = u_r^2(d) + u_r^2(\sec(\theta)) + C_{\alpha_m}^2 u_r^2(\cos(\alpha_m)), \quad (3)$$

where the symbol u_r denotes the relative standard uncertainty of the quantity in parentheses and where the absolute value of the sensibility coefficient for the divergence angle

$$C_{\alpha_m} = -\frac{1 + 2\cos(\alpha_m)}{(1 + \cos(\alpha_m))\,(1 + \cos(\alpha_m) + \cos^2(\alpha_m))} \quad (4)$$

is very close to $1/2$ in the small angle approximation.

3.2.1. UV Beam

The beam inclination has been determined by observing the reflections from the cell windows using a superposed HeNe beam. From repeated measurements, $\theta = (3.9 \pm 0.1)^{\circ}$ has been found. However, most of the uncertainty comes from co-aligning the HeNe and the UV beam. It is conservatively estimated that the superposition can be achieved with an accuracy of ±2 mm (uniform probability) at either side of the cell (at 58.8 mm outer window distance). Using a Monte-Carlo simulation ($N = 10^8$), we find $\sec(\theta) = 1.00270 \pm 0.00138$, thus $u_r(\sec(\theta)) = 1.38 \cdot 10^{-3}$.

The divergence angle has been determined from the apertures of the entrance and the exit of the overall optical system, that otherwise only contains plane optical elements. The entrance diameter (iris) was set at $D_a = 4$ mm and the detector was installed behind a $D_b = 12.7$ mm diameter lens. Since these two elements were separated by the distance of $l = 355$ mm, α_m is confined to the range between 0 and

$$\alpha_> = \arctan\left(\frac{D_a + D_b}{2l}\right), \quad (5)$$

which amounts to $\alpha_> = 1.35^{\circ}$. This implies $\cos(\alpha_m)$ being between 1 and $1 - 2.77 \cdot 10^{-4}$. Assuming a rectangular probability distribution function (PDF), we have the best estimate $\cos(\alpha_m) = 1 - (1.38 \pm 0.80) \cdot 10^{-4}$ and $u_r(\cos(\alpha_m)) = 8.0 \cdot 10^{-5}$.

Following Eqs. (2) and (3), this results in an effective absorption length of $L_{UV} = 50.961(72)$ mm with a relative standard uncertainty $u_r(L_{UV}) = 1.41 \cdot 10^{-3}$. The latter is entirely dominated by the uncertainty associated to the determination of the beam inclination with respect to the cell windows.

3.2.2. IR Beams

The geometric parameters of the two IR beams are based on direct interferometric length measurements on the one hand and on the determination of the angular parameters using millimeter paper and calipers on the other hand. To this end, the cell was illuminated with the thermal source of the measurement configuration. This allowed to visually inspect limitations of the azimuthal beam symmetry. Both IR beams are focalized onto the centers of the two cells, and the convergence angle α_m has been determined from comparing the beam diameters at the two ends of the sample compartment using Eq. (5).

The beam centers on both sides of the long cell were displaced with respect to the window centers by 6 mm in the vertical and 2 mm in the horizontal direction over the outer cell length of 204 mm. It is assumed that beam centers could be determined within a uniform uncertainty interval of ±2 mm in both directions. Using these parameters in a Monte-Carlo simulation ($N = 10^8$), we find $\sec(\theta) = 1 + 4.87 \cdot 10^{-4}$ with a relative standard uncertainty of $u_r(\sec(\theta)) = 1.22 \cdot 10^{-4}$.

The divergence angle has been determined from the measurement of the optical length in the sample compartment $l = (306 \pm 2)$ mm and the horizontal $D_h = (23 \pm 1)$ mm and vertical $D_v = (19 \pm 1)$ mm extent of the beam. Originally, the beam is circular, but optical elements cut off some portions at the upper and lower beam edges. Calculating α_m using either $D_h + 1$ mm or $D_v - 1$ mm gives reasonable upper and lower values for the effective beam length due to divergence. Using Eq. (5) with $D_a = D_b = D_v - 1$ mm and $D_a = D_b = D_h + 1$ mm, $\alpha_m = 3.93^{\circ}$ and $\cos(\alpha_m) = 0.99765$ with a relative standard uncertainty of $u_r(\cos(\alpha_m)) = 3.86 \cdot 10^{-4}$ is found.

Taking these results together (see Eqs. (2) and (3)), this leads to an effective length $L_{IR,l} = 200.357(66)$ mm for the long IR path with a relative standard uncertainty of $u_r(L_{IR,l}) = 3.3 \cdot 10^{-4}$.

The short path has the same divergence as the long path, thus $\cos(\alpha_m) = 0.99765 \pm 0.00039$. For the inclination θ, we find that the beam is displaced with respect to the window centers by 2 mm and 0 mm in the horizontal and vertical directions, respectively. These shifts are

observed on the windows' outer faces at a distance of about 59 mm. A Monte-Carlo simulation ($N = 10^8$) using these parameters yields $\sec(\theta) = 1+7.71\cdot10^{-4}$ with a relative standard uncertainty of $u_r(\sec(\theta)) = 4.99 \cdot 10^{-4}$.

Combining this with above results on the length measurement, an effective short path length $L_{IR,s} = 50.919(31)$ mm with a relative standard uncertainty of $u_r(L_{IR,s}) = 6.0 \cdot 10^{-4}$ is found. This and all other length measurements are summarized in Table 3.

3.2.3. Multiple reflections

Geometric lengths of the absorption paths have been calculated neglecting back reflections from windows, filters and the interferometer optics that are essentially perpendicularly orientated with respect to the optical axis and could reflect back on another surface from which the light passes onto the detector. While of general concern in spectroscopic photometry [45] and FTIR spectroscopy [46], these effects are rarely quantified in FTIR studies and we therefore discuss this issue in some detail. Concerning ozone, such effects have been discussed in UV absorption measurements considering the case of a collimated beam traversing the two parallel windows of an absorption cell [2, 18], where multiple reflections between these two windows lead to a systematic overestimation of the absorbance, if neglected. A remedy is to use antireflection coatings or to incline the collimated beam with respect to the optical cell axis. The inclination leads to an offset of the reflected beams exiting the cell which can be filtered out when the beam diameter is sufficiently small. This approach has been chosen for the UV beam, but it has not been feasible for the IR beams due to the geometry imposed by the spectrometer, where four windows are mounted approximatively perpendicular to the optical axis behind the interferometer unit: the two cell windows, the filter, and the detector window. All filters and windows in the light path are wedged at small angles between 0.17° and 1.15° and the cell windows have additionally been inclined by 1.7° to 2.2°. In addition of light being reflected between window surfaces behind the interferometer unit, back reflections from these surfaces into the interferometer also need to be considered.

In analogy to Hodges et al. [18], the effect of back reflections on the absorbance measurement in the presence of more than two windows or reflective elements is described by the following equation:

$$\begin{aligned}\frac{\Delta A}{A} &\simeq \frac{1}{A}\ln\left(\frac{1+\sum_{i\neq j}\omega_{i,j}\tau_{i,j}^2R_iR_j}{1+e^{-2A}\sum_{j>1}\left(\omega_{0,j}\tau_{0,j}^2R_0+\omega_{1,j}\tau_{1,j}^2R_1\right)R_j+\omega_{0,1}\tau_{0,1}^2R_0R_1+\sum_{j>i>1}\omega_{i,j}\tau_{i,j}^2R_iR_j}\right)\\ &\simeq \frac{1-e^{-2A}}{A}\sum_{j>1}\left(\omega_{0,j}\tau_{0,j}^2R_0+\omega_{1,j}\tau_{1,j}^2R_1\right)R_j, \end{aligned} \quad (6)$$

where $\Delta A/A$ is the relative difference between measured and actual gas absorbance A and where we consider and keep only lowest order terms that are quadratic forms in the reflection coefficients R_i. Corresponding to our geometry, we have designated by R_0 the reflectivity of the interferometer and by R_1 the reflection coefficient of the entrance cell window. R_2 to R_5 are reflection coefficients of the exit cell window, the interference filter, the detector window, and the detector element, respectively. The transmittances $\tau_{i,j}$ between optical elements i and j for a collimated beam can be calculated as products of transmittances $(1 - R_k)$ of all windows $i < k < j$ that are passed when the beam is propagating between elements i and j (assuming negligible absorption and scattering). The geometrical factors $\omega_{i,j}$ take into account deviations from the collimated beam geometry and correspond to the fraction of the retro-reflected light falling onto the detector. As an aside, note that for $\omega_{1,2} = \tau_{1,2}^2 = 1$ and considering only two windows with coefficients $R_1 = R_2 = R_e$, our Eq. (6) corresponds to the first order development in R_e^2 of Eq. (3) given by Hodges et al. [18]. Interestingly, only back reflections that traverse the gas cell (reflections from elements 2 to 5 followed by back reflection from the interferometer or the first cell window) contribute in Eq. (6), because for all other combinations quadratic terms in the nominator and denominator are identical and cancel in the lowest order approximation. Moreover, the A-dependance can be factored out as a pre-factor (see Eq. (6)) and describes a non-exponential decay yielding a factor of 2 in

Table 4: Quantification of the relative augmentation of the effective absorption effective path due to multiple reflections. Back reflection into the interferometer (FT) is described by a global estimate in the first line. Back reflections from the entrance cell window are calculated according to Eq. (7). All values are given in percent (%). Numbers in parentheses indicate standard uncertainties in units of the last digit.

	5 µm				10 µm			
back reflection	$\omega_{1,j}$	$\tau^2_{1,j}$	R_1R_j	contribution to $\Delta l/l$	$\omega_{1,j}$	$\tau^2_{1,j}$	R_1R_j	contribution to $\Delta l/l$
FT - (cell, filter & detector)	—	—	—	0.000(465)	—	—	—	0.000(577)
cell - cell	0.00(000)	100.0	0.631	0.000(000)	0.09(032)	100.0	0.316	0.000(001)
cell - filter	1.47(109)	84.8	3.216	0.059(043)	12.1(094)	89.1	0.351	0.038(029)
cell - det. window	9.99(673)	30.0	0.432	0.010(007)	14.1(153)	78.3	1.641	0.181(197)
cell - det. element	1.16(124)	26.8	0.171	0.001(001)	07.3(140)	39.2	2.021	0.058(112)
all				0.070(468)				0.277(669)

the case of small absorbances ($A \to 0$) and vanishing for $A \to \infty$. Thus treating the absorbance of an individual line as a random variable and assuming a rectangular probability distribution of the A dependent term, we obtain a global simplified expression for the prolongation of the absorption path which is independent of the particular absorption that we are considering

$$\frac{\Delta L}{L} = \sum_{j>1} \left(\omega_{0,j} \tau^2_{0,j} R_0 + \omega_{1,j} \tau^2_{1,j} R_1 \right) R_j. \qquad (7)$$

A relative standard uncertainty due to the choice of the pre-factor $u_r(f(A)) = 1/\sqrt{3} = 0.577$ must be added to contributions due to the other quantities in Eq. (7). Compared to this rough approximation and uncertainties related to the beam geometry, refractive index data of common window materials (KBr and BaF_2 for the cell windows and CaF_2 and ZnSe for the detector windows at 5 µm and 10 µm, respectively [47–49]) are so accurate that only uncertainties in the $\omega_{i,j}$-values need be considered here. Back reflections involving the entrance window have been determined from known reflection coefficients, respective refractive indices and geometric factors using the spectrometer and cell geometry. The cell inclination of the long arm as indicated in Section 3.2.2 has been used as a reference. Orientations and window wedges of the short arm have been determined in a separate experiment with the cell removed from the spectrometer using reflections of a laser beam aligned along the long cell axis. This measurement revealed that the short cell is vertically and horizontally inclined by 0.9° and 0.2°, respectively and that the cell windows had horizontal wedges of 0.75° at the front and vertical wedges of 0.75° at the back of the cell. The laser measurements were made after removing the cell from the spectrometer, however, without having determined if the horizontal inclinations and wedges add to the inclination of the long cell inclination or not. This uncertainty has been considered in the determination of the geometric factors using a Monte-Carlo simulation based on matrix based ray tracing calculations considering all possible geometric configurations and the uncertainty of the inclination measurements. In these simulations all windows and filters except the cell entrance and exit windows have been considered to be parallel and perpendicular to the light path, resulting in a conservative estimate. Geometric factors $\omega_{1,j} < 1$ are mostly due to the fact that back reflections increase the image of the spectrometer entrance in the centre of the cell, leading to a spot size exceeding the detector element size (1 mm × 1 mm) following the 3:1 image scaling of the spectrometer optics. Depending on the defocalization, this effect is largest for the cell-cell reflection and smallest for back reflection from the detector window. The simulation has taken into consideration the possibility that the spectrometer has not been aligned perfectly: up to 30% loss due to defocalization or shift of the focal point with respect to the centre of the detector has been allowed for by accidentally varying these parameters during the Monte-Carlo runs. The results of these runs and the properties of the optical elements are summarized in Table 4.

A different approach needed be chosen for determining back reflections into the interferometer, because these depend critically on the alignment of the interference filters. An inclination of only 0.3° decides whether light is back-reflected into the interferometer or blocked out by the exit aperture. We have therefore analyzed saturated N_2O spectra for the presence of double-modulation artifacts due to back-reflection into the interferometer [50, 51]. By comparing the frequency doubled spectrum with the noise level in the double modulation region, upper limits of 2‰ and 2.5‰ could be derived for the fraction of the double modulated signals at 5 µm and 10 µm, respectively. This corre-

sponds to respective maxima of 0.8% and 1% of back-reflected signal in the singly modulated region of the spectrum. Since we are limited by the detection level of our analysis and the actual level might be much smaller, we assume a negligible (= 0) level of interferometer back reflections, but use corresponding uncertainties of $0.008/\sqrt{3} = 0.00465$ and $0.01/\sqrt{3} = 0.00577$ at 5 µm and 10 µm, respectively. When occurring before the absorption cell, back reflections into the interferometer lead to a diminution of the absorption signal and induce a negative bias. If the reflection takes place behind the cell, however, additional cell passages will overcompensate this negative bias and the positive error limit applies. A priori we don't know where such reflections happen. This provides an additional rationale for not applying a systematic correction.

The overall prolongation of the absorption paths is indicated in the last line of Table 4 and the resulting path lengths are summarized in Table 3.

3.3. Ozone absorption cross section at 253.65 nm

A pen ray lamp in combination with two 10 nm wide (FWHM) interference filters has been used to generate the 253.65 nm mercury line emission, which was then used to measure the ozone amount in the short path cell by UV absorption. A UV fiber was employed to separate the hot pen ray lamp outside the FTS from the optical and opto-mechanical elements in the spectrometer compartment, where the H-cell has been located. The UV absorption cross section has been revised recently based on a literature review and a new consensus value $\sigma_{UV} = 1.1329 \cdot 10^{-17}\,\mathrm{cm}^2$ has been identified [18]. We have made use of this most recent recommendation. Its relative standard uncertainty $u_r(\sigma_{UV}) = 3.1 \cdot 10^{-3}$, which includes systematic biases, is about 10 times smaller than the value of Hearn [19] and 2 times smaller than the often used value of Mauersberger et al. [4].

3.4. UV Absorbance

UV absorbance measurements were operated continuously during the measurements. The UV absorption setup based on a measurement and reference beam configuration required that UV measurements of the empty cell were taken before and after the measurement. This allowed to determine the zero absorption level. Due to the long measurement period, small instrumental drifts and measurement noise, the two calibrations yielded slightly different results. The absorbance measurement has been determined from weighting the two calibrations as a function of time, the first being valid at the start of the measurement and the second at the end and intermediate times being linearly interpolated between these two cases. This yields the average ozone pressure essentially as the arithmetic mean of the two calibrations and its uncertainty can be derived from the observed deviation of either calibration from the mean value. For the four runs, the so obtained uncertainty varied between 0.06% and 0.20% and was largest for the high pressure measurement where the absorption signal was reduced due to the very strong absorption. We conservatively assign this value $u_r(A_{\mathrm{UV}}) = 2.0 \cdot 10^{-3}$ as uncertainty for all our UV measurements.

3.5. Temperature

Two thin film Pt100 temperature sensors have been diagonally attached to the outside of the two parallel cells close to the windows. The temperature sensors have been compared to a Platinum reference thermometer and were calibrated to better than ±0.05 K, using a setup described previously [44]. During the measurement, temperature readings showed a slow evolution in time and gradients between the two sensors. Spatial gradients never exceeded 0.16 K during all runs and the temporal variation remained always within 0.81 K. The maximum observed temperature difference (spatial and temporal) within a run ranges from 0.16 K to 0.89 K. It has been obtained from the temperature maximum of the first sensor with respect to the lowest temperature observed by the second sensor or vice versa, whichever difference was largest. Conservatively, we chose the value of 0.89 K as representative for our measurements. Assuming rectangular probability distributions for the temperature uncertainty due to the calibration and the maximum observed gradient of temperatures in both space and time, we arrive at a standard temperature uncertainty $u(T) = \sqrt{(0.89^2 + 0.10^2)/12}\,\mathrm{K} = 0.26\,\mathrm{K}$, which corresponds to a relative standard uncertainty of $u_r(T) = 8.7 \cdot 10^{-4}$.

3.6. Gas purity and isotopic composition

High purity research grade (99.9995%, Alphagaz 2, Air Liquide) oxygen has been used to generate ozone in a glass vacuum system with only few metal bearing components (pressure gauge, pump, etc.). No attempt has been made to determine accurately the sample purity. Instead, the instantaneous ozone abundance has been measured in-situ during the spectrum recordings. The observed low ozone decomposition times are indicative of very low concentrations of reactive species. Spatial and temporal gradients of ozone and impurities in the present set-up are a concern and are discussed hereafter. The isotopic composition of the ozone gas

has also not been determined directly, but since oxygen gas is usually obtained by liquefaction of air through the Hampson-Linde cycle in industrial air separation units, the ozone isotopic composition can be inferred with sufficient accuracy.

3.6.1. Concentration gradients

The UV based determination of the ozone abundance in the intensity measurements assumes that molecules are well mixed over all parts of the H-shaped absorption cell and that impurities, mostly molecular oxygen from the decomposition of ozone, are also homogeneously distributed over the cell volume. Gradients of such impurities could lead to a bias in the determination of the ozone partial pressure, because the different absorption paths do not coincide. However, spatial gradients in ozone number density are negligible under the experimental conditions with total pressures between roughly 0.22 hPa and 1.58 hPa, because diffusional time scales are short. The largest span in the cell is from a window surface of the short cell arm to one of the window surfaces in the long cell. It amounts to about $l = 41$ cm. The temporal time scale for free molecular diffusion is given by

$$\tau_d = \frac{l^2}{4D}, \tag{8}$$

where D is the diffusion coefficient. Using Lennard-Jones parameters from Kaye [52], the $T = 298$ K coefficients for the diffusion of O_2 in pure O_3 are $D = 703\,\mathrm{cm^2\,s^{-1}}$ at 0.22 hPa and $D = 100\,\mathrm{cm^2\,s^{-1}}$ at 1.54 hPa [53]. This indicates diffusional time scales between 0.6 s and 4.2 s. Compared to free space, however, diffusion in the cell is slowed down due to the presence of wall boundaries. In order to obtain a more realistic estimate of diffusional time scales for the given geometry as well as for reasonable scenarios of the observed ozone loss, we have performed Monte-Carlo simulations for two different settings. The simulations were based on a simple hard sphere collision model using Lennard-Jones potential parameters to derive impurity redistribution times for the two low pressure experiments, where the free space diffusional time constant are 0.6 s and 1.2 s, respectively. In one type of simulation, we assume that ozone exclusively decomposes in the volume directly irradiated by the UV beam; in the other we suppose that decomposition occurs just on the surface of one of the windows of the long cell. Both simulations yield exponential time scales for the redistribution of O_2 over the entire cell volume of 1.7 s and 3.6 s for the two different pressures, respectively. This indicates a geometry related reduction of the free space diffusional time scale by a factor of 3. Using this scaling factor, we obtain $\tau_d \sim 13$ s for $D = 100\,\mathrm{cm^2\,s^{-1}}$ as an upper limit for the diffusion time of all our measurements. The identical time scales for the two different scenarios are consistent with the diffusion from one cell arm into the other being the time controlling step, whereas redistribution within each arm is considerably faster. At 1.54 hPa, radial distribution occurs within a few milliseconds and longitudinal diffusion in the long and the short cylindrical arms takes 1 s and 0.06 s, respectively. These times are so short that ozone decomposition cannot lead to the buildup of significant concentration gradients.

Supposing that all decomposition of ozone occurs on a single window in the long arm, ozone in that arm will be lost at the rate $-[O_3]\gamma_L/\tau_l$, where $\gamma_L = V/V_L = 2.21$ is the ratio of the cell volume over the long arm volume and τ_l the time constant of the loss. As a consequence of the local decomposition of ozone, a concentration gradient between the arm and the rest of the cell will build up until it is counterbalanced by the diffusional flow driven by the same gradient $(-\Delta[O_3]/\tau_d)$. Consequently, a dynamic equilibrium is established with a relative concentration gradient of $\Delta[O_3]\big/[O_3] \simeq \gamma_L(\tau_d/\tau_l)$. Under our conditions, $\Delta[O_3]\big/[O_3]$ is less than 3 µmol/mol.

Using the same argument, we obtain gradients on the order of 400 µmol/mol, when the observed ozone decomposition is assumed to exclusively occur in the cylinder formed by the 4 mm circular diameter UV beam passing through the short cell. The higher value is due to the elevated ratio of volumes $\gamma_{UV} = V/V_{UV} = 375$ in this case. However, this scenario must be excluded because of the low UV beam power around 1.2 nW. Assuming complete absorption and taking into account the quantum efficiency of 5.7 for ozone decomposition in pure O_3 at 254 nm [54], photolytic ozone decomposition occurs at a maximum rate of $J = 8.7 \cdot 10^9\,\mathrm{s^{-1}}/N = 1.0 \cdot 10^{-9}\,\mathrm{s^{-1}}$, using $N = 8.7 \cdot 10^{18}$ ozone molecules in the cell. This is more than two orders of magnitude slower than the observed ozone decomposition rate. Therefore, photolytically generated gradients must be lower than the previously calculated number by at least two orders of magnitude and cannot exceed the 4 µmol/mol range when comparing the two cell arms. They must be even smaller when comparing the 10 µm IR beam to the UV beam, as both beams pass the short cell at a small distance on approximately parallel paths. The most probable scenario for explaining the observed ozone decomposition in the cell is that wall assisted decomposition occurs at several spots all over the cell, implying that concentration gradients are likely smaller than 10^{-5}. Given the uncertainties in the determination

of the ozone amounts on the relative level of a few 10^{-3}, gradients below 10^{-5} relative can be safely ignored.

Even though the high pressure run has been used to determine the photolysis rate, not much of the argument changes even in the low pressure run, because only 23% of the photons are absorbed in this case. The corresponding photolytic decomposition rate is $1.9 \cdot 10^{-9}$ s^{-1} and still remains more than two orders of magnitude lower than the observed ozone loss. At the same time the diffusional time scale is seven times smaller than at the highest pressure, leading to a much faster reduction of gradients. Finally, it should be noted that the time constant of ozone decomposition of more than 23 days is considerable and likely achieved in only few spectroscopic measurements.

We have also analyzed ozone losses within the long absorption cell using the spectra at 5 µm. Derived loss rates vary from $-2.7 \cdot 10^{-7}$ s^{-1} to $-5.0 \cdot 10^{-7}$ s^{-1} and are fastest at the lowest pressure. On average, these relative loss rates are smaller than the corresponding UV derived rates (see Table 2) by $0.1 \cdot 10^{-7}$ s^{-1}, but the difference is insignificant and well within the 95%-confidence interval of $\pm 0.5 \cdot 10^{-7}$ s^{-1}. Given the smallness of decomposition rates, the comparison cannot provide additional information on whether the ozone molecules are lost all over the cell volume or only at some localized positions, but it independently confirms that the same slow bulk decomposition of ozone is observed in both cell arms.

3.6.2. Isotopic composition

The relative abundance of the ozone main isotopologue can be calculated as (see Appendix B)

$$r_{666} = \left(1 + R^{18}_{\mathrm{VSMOW}}\left(1 + \delta^{18}\right) + R^{17}_{\mathrm{VSMOW}}\left(1 + \delta^{17}\right)\right)^{-3}, \quad (9)$$

where the isotope ratios R and δ-values for the rare ^{17}O and ^{18}O isotopes are defined as in Appendix B. Its relative uncertainty $u_r(r_{666})$ is well approximated by $3R^{18}_{\mathrm{VSMOW}}\, u(\delta^{18})$ (see Eq. (B.2)). δ-values are typically small and describe the relative deviation of the isotopic composition of the ozone sample from the composition of the reference material VSMOW (Vienna Standard Mean Ocean Water). In what follows, δ is calculated in two steps. First the isotope composition of the oxygen gas (δ_g) is estimated. Then the isotope fractionation that occurs in the formation of ozone (ϵ_f) is considered, such that $1 + \delta = (1 + \epsilon_f)(1 + \delta_g)$.

Because we had no means to determine the isotopic composition of our tank oxygen, we undertook a non-exhaustive survey of published data on O_2 working standards and on commercial O_2 gas cylinders used by laboratories which have specialized in the three isotope analysis of O_2 between 1983 and 2019. This is assumed to be a good indication of the composition and expected variability. 15 different data sets had been identified, all displayed in Table 5. With the exception of one gas sample, δ-values are positive, which is expected from the offset of atmospheric oxygen from ocean water [68]. The arithmetic mean of these 14 samples (excluding the negative outlier) is δ^{18}O = 22.5 ‰ and δ^{17}O = 11.6 ‰. Median values of all data are just slightly higher at δ^{18}O = 23.5 ‰ and δ^{17}O = 12.4 ‰, with both averages being close to the isotope composition of air oxygen (δ^{18}O = 23.88 ‰ and δ^{17}O = 12.08 ‰ [69]). We speculate that the negative sample has been obtained from a different technique of oxygen production, such as water electrolysis. Small sample debiased standard deviations are $u(\delta^{18}_g)$ = 18.3 ‰ and $u(\delta^{17}_g)$ = 9.6 ‰. Since our oxygen likely is somewhere in the range covered by the data in Table 5, we adopt $\delta^{18}_g = (22.5 \pm 18.3)$ ‰ and $\delta^{17}_g = (11.6 \pm 9.6)$ ‰, noting that with the exception of the one negative data point, all data are within $\pm 1.3\, u(\delta_g)$ of the mean value.

Table 5: Oxygen isotopic composition of O_2 working/tank gases in mass spectrometer laboratories around the world. δ values are given with respect to VSMOW. Two of the reference gases (indicated by an asterisk) had only the ^{18}O-content reported. In these cases, ^{17}O has been inferred using standard scaling $\delta_g{}^{17}\mathrm{O} = 0.528 \times \delta_g{}^{18}\mathrm{O}$ [55].

No.	$\delta_g{}^{18}$O / ‰	$\delta_g{}^{17}$O / ‰	Year	Reference
1	46.1	24.1	1995	[56, 57]
2⋆	45.5	23.9	1991	[58]
3	41.8	21.8	1999	[59, 60]
4	38.7	19.5	2009	[61]
5	27.54	14.02	2013	[62]
6	27.1	13.79	1995	[56, 57]
7	24.58	12.48	2003	[63]
8	23.5	11.87	1983	[64]
9⋆	23.4	12.4	1991	[58]
10	18.542	9.25	2019	[65]
11	14.6	7.8	1995	[56, 57]
12	12.1	6.0	2009	[61]
13	11.986	5.906	2016	[66]
14	4.4	2.2	1998	[55]
15	−21.72	−11.5	2016	[67]

Large additional isotope fractionation occurs when ozone forms from molecular oxygen [70–72]. This leads to isotopologue specific enrichments or depletions of up to 20% [73], depending on temperature and pressure [74]. Depletions are associated with the rapid isotope exchange between O atoms and O_2 molecules and become dominant at low pressures and temperatures

when ozone forms at the reactor surface. Enrichments occur in the association of O to O_2 in the gas phase [72], which depending on the reactor size is typically dominant at pressures above 50 hPa [75]. In our system, ozone is formed via electric discharge in a cylindrical glass reactor of 50 mm diameter, immersed into liquid nitrogen. At liquid nitrogen temperatures and without walls, isotope enrichments of ozone with respect to initial oxygen should be slightly negative (ϵ_f^{18}) or around zero (ϵ_f^{17}) [75, 76], but observed fractionation constants can be higher (roughly between 25 ‰ and 40 ‰ [64]), likely due to the effective temperature in the discharge being higher than the environment. Similarly, fractionation constants of ozone generated at room temperature by electric discharge are always higher by 20 ‰ to 30 ‰ compared to photolytically recycled ozone [75], despite visible light photolysis leading to a slight additional enrichment in heavy ozone isotopologues [77]. We therefore can safely assume an upper limit for the instantaneous fractionation constants $\epsilon_f^{17} = \epsilon_f^{18} = +40\,‰$. Because isotopic depletions occur, particularly in small reactors at low temperatures, we deduce from the low temperature measurements of Janssen and Tuzson [74] lower limit values of −100 ‰ for ^{18}O and −50 ‰ for ^{17}O. Here, at least 50% of the O_2 has been converted into O_3. Mass conservation requires that the bulk ozone isotopic composition is less fractionated then the reported instantaneous fractionation constant. Applying the corresponding Rayleigh formalism [78] yields a reduction of the instantaneous fractionation by a factor of ln(2) = 69.3%. ϵ_f^{18} may thus be anywhere between −69 ‰ and +27 ‰ and ϵ_f^{17} could take any value from −35 ‰ to +27 ‰. Assuming a rectangular probability distribution function within these margins yields $\epsilon_f^{18} = (-20.8 \pm 28.0)\,‰$ and $\epsilon_f^{17} = (-3.5 \pm 18.0)\,‰$ so that we finally obtain $\delta^{18} = (1.2 \pm 33.8)\,‰$ and $\delta^{17} = (8.1 \pm 20.6)\,‰$ when combining with the estimate for the isotope composition of our oxygen gas.

With known fractionation constants at hand and the composition of VSMOW given in Appendix B, the relative abundance of the main ozone isotopologue is $r_{666} = 0.9929$ with a standard uncertainty $u(r_{666}) = 0.0002$ (see Eqs. (9) and (B.2)). This value coincides with the isotopologue abundance $r_{666} = 0.992901$ in the HITRAN database.

3.7. IR Transmittance measurements

Several factors contribute to the uncertainty of the absorbance or transmittance measurements, such as photon and detector noise, detector non-linearity and thermal emission of the sample and the cell. These different effects will be discussed in the following. Their impact on the line intensity measurements will be presented later in Sec. 3.8.3.

3.7.1. Detector and photon noise

Inspection of absorption free spectral ranges in the two spectral regions indicates signal to noise ratios of 120 (peak to peak) at 10 µm and 350 at 5 µm, and roughly five times higher ratios (600 and 1800) if the noise is expressed in terms of RMS signal. We derive relative noise levels of $u_{r,D}(\tau) = 1.7 \cdot 10^{-3}$ and $u_{r,D}(\tau) = 5.6 \cdot 10^{-4}$ at 10 µm and 5 µm, respectively. The impact on the intensity measurements will be quantified in Sec. 3.8.3.

3.7.2. Detector non-linearity

The non-linearity of IR detectors is a viable concern in quantitative absorption measurements [79–81]. In particular MCT (or HgCdTe) detectors are known for their non-linear behavior [82, 83] and several methods have been proposed to avoid [80, 82], detect [80–82, 84] or correct for [84–86] it. We have adopted the correction scheme proposed by the FTS manufacturer [85] for two reasons. First, the algorithm has been successfully applied to quantitive FTIR spectroscopy in the past [79]. Second, application of the correction in the spectral domain at 10 µm leads to efficient removal of baseline effects. No correction was required in the 5 µm region, because InSb detectors that are used in this region typically have excellent linearity properties [87, 88]. Indeed, the measurements of Boivin [88] indicate that over one decade of intensities, transmittances can be measured at better than 10^{-3}, yielding a standard uncertainty $u_{r,nl}(\tau) = 5.8 \cdot 10^{-4}$. As expected, saturated absorption spectra of N_2O acquired at 5 µm, showed a flat zero baseline.

In general terms, when the sensitivity of a photodetector depends on the photon flux density, the detector is non-linear. In MCTs, saturation effects occur at higher photon flux densities [83, 89], but other effects might contribute such that the recorded interferogram must be represented as a power series in the undistorted interferogram [82, 84, 90]. If the higher order terms cannot be rendered negligible by physical means (reduction of the photon flux, ...), the second or even the next higher interferogram order terms can be taken into account for correcting the measurement. The measured spectrum which is obtained as Fourier transform of the interferogram will correspondingly be given as a linear combination of the zeroth, first and higher order autocorrelation functions of the undistorted spectrum. While the use of a perfectly linear detector would imply that the

first and higher order spectral autocorrelation terms disappear, the presence of these terms leads to in and out of band artifacts. The spectral artifacts are most noticeable through their effect on the zero-transmission baseline that translate into systematic bias in the retrieval of line intensities or deviation from the Lambert-Beer law [82, 90, 91]. The stronger the line intensity and the absorption signal, the stronger is the impact of the non-linearity related baseline bias. Correspondingly, a zero baseline at zero spectral transmission therefore indicates the absence of detector non-linearity, or in the case of a rectified spectrum that it has been corrected successfully [81, 90, 92].

In order to observe any baseline effect in the spectral region of interest, an almost saturated ozone spectrum of about 80 Torr (107 hPa) has been recorded. The ozone pressure has not been high enough to completely saturate the spectrum over a broader range, but it could not be further increased due to safety considerations. Nevertheless, as can be seen from Fig. 3, transmission levels were close to zero and flat in individual micro-windows of several ~0.01 cm^{-1} width around the strongest absorption lines. In these ranges, a simulated spectrum provides a good proxy for the saturated transmission baseline. Numerical tests have shown that simulated spectra in these flat regions at the 10^{-3} transmission level were very insensitive to the width of the instrument line function (on the order of 10^{-4} when the resolution is changed by 10%) or when the pressure is altered. Nine of such windows with a spectral width of several 0.01 cm^{-1} have been identified. The average deviation between the measured and calculated spectra has been used as an indicator for the presence of detector non-linearity (see Table 6). It is evident that the correction improves the agreement with the theoretical prediction by one to two magnitudes. Transmittance deviations are within a few 10^{-4} and range from $-4.3 \cdot 10^{-4}$ to $+5.0 \cdot 10^{-4}$. The average obtained when values are weighted by the window widths is $\langle \Delta(\tau) \rangle = (-0.3 \pm 1.5) \cdot 10^{-4}$. These values indicate a very high degree of linearity and are smaller than typical characteristics [87, 88] of InSb detectors (see above). We conservatively chose $u_r(\tau) = 5.8 \cdot 10^{-4}$ for both wavelength regions. The results also imply that eventual non-linearities introduced by the detector or acquisition electronics can be neglected, irrespective of the wavelength range. This is because we can assume that being from the same producer, both detector electronics have undergone the same level of sophistication in the development and quality control.

Another consequence of the results presented in Table 6 is that correction for non-linear detectors is essen-

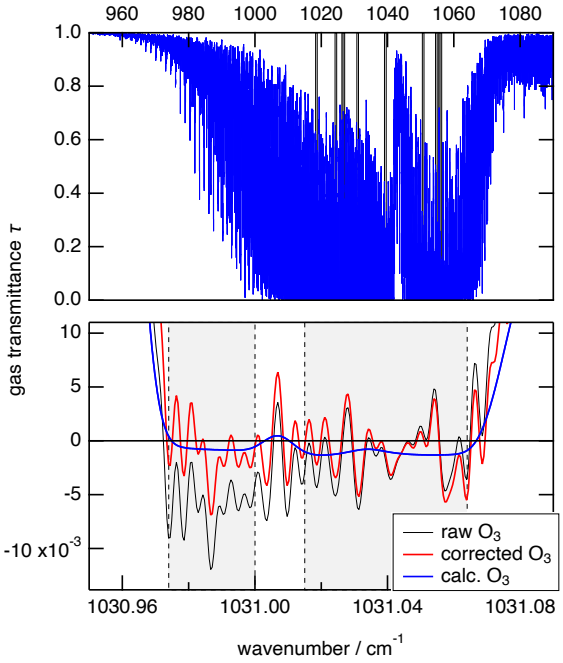

Figure 3: Saturated ozone spectrum in the 10 µm region. The top window shows a simulated absorption spectrum at ~ 107 hPa (80 Torr) of ozone over an absorption length of 50.9 mm. Micro-windows selected for analysis are indicated by shaded regions with displayed widths (0.5 cm^{-1}) not being to scale for reasons of clarity. The lower panel zooms at the micro window at 1031.02 cm^{-1} in the maximum of the *P*-branch, separated into two distinct sub-windows that are indicated by grey shades. The uncorrected or raw (black line) and the corrected (thick red line) FT spectra are compared to the calculated spectrum (thick blue line) in the rather flat baseline range.

Table 6: Deviation of measured from expected signal at saturation (107 hPa of ozone at room temperature). Deviations are obtained as average transmittance differences in micro-windows where expected ozone absorption spectra are flat. Values are given for corrected ($\Delta(\tau)$) and uncorrected ($\Delta'(\tau)$) spectra. p-sensitivity values are expressed as change in $\Delta(\tau)$ when the nominal pressure alters by 1%. Micro-windows indicated by a $\star$-symbol have been obtained by summing two or more nearby sub-micro-windows for analysis (see Fig. 3, for example).

Micro-window			$\Delta(\tau)$	$\Delta'(\tau)$	p-sensitivity
No.	Position (cm^{-1})	Width (cm^{-1})	(10^{-4})	(10^{-4})	(10^{-5}/%)
1	1018.564	0.021	4.99	-85.24	-0.02
2	1024.419	0.027	1.32	-57.50	0.62
3$\star$	1027.120	0.096	-1.51	-27.56	-1.25
4$\star$	1031.064	0.075	-0.13	-19.81	1.18
5	1039.360	0.034	-3.95	-57.22	-1.35
6$\star$	1050.796	0.045	-4.25	-62.17	0.18
7$\star$	1054.795	0.047	3.19	-84.15	1.21
8	1055.721	0.044	3.85	-133.60	-0.16
9$\star$	1056.260	0.079	0.84	-5.83	-0.79

tial for quantitative FTIR analysis. As shown by comparison of the uncorrected spectrum with the baseline $\Delta'(\tau)$ in Table 6, biases of up to ca. 1% are observed in our spectroscopic setup when no such correction is applied. The micro-windows have also been selected for the low sensitivity of the baseline towards pressure changes. Since the pressure has been determined by a capacitive gauge that had not been calibrated recently, we assume that the pressure had been somewhere in the range of (80 ± 5) Torr or (106.7 ± 6.7) hPa, corresponding to a relative standard uncertainty of 3.6%. The effect of the pressure uncertainty on our analysis therefore is ten times smaller than the level of uncertainty linked to detector non-linearity.

3.7.3. Thermal emission

As shown by Ballard et al. [93], the ratio S_g/S_e of the spectrum of the absorption cell with gas (g) divided by the spectrum without gas (e) does not yield directly the gas transmittance τ. Instead, the thermal emission of the gas sample contributes to the signal. The factor by which S_g/S_e deviates from the pure gas transmittance τ is given by:

$$\frac{S_g}{S_e} \simeq \left[1 - \epsilon \frac{(1-\epsilon_w)B(T_c)\tau_w D_d^2}{B(T_s)D_s^2}\right]\tau, \qquad (10)$$

where $B(T)$ is the Planck function at temperature T, τ_w and ϵ_w are the transmittance and the emissivity of a single cell window, respectively. ϵ is the emissivity of the gas and D_s and D_d are the respective diameters of the entrance and exit apertures of the interferometer. All quantities in Eq. (10) except the diameters are wavenumber (ν) dependent. Our expression corresponds to the original Eq. (4) in [93] with the exception of the solid angles that cancel and the throughput areas which were replaced by the iris diameters. Note that we have measured $D_d/D_s = 1.12$, which is close to the nominal value of 1.13. The effect of thermal emission can be corrected directly by using different globar or source temperatures when recording full and empty cell spectra, but this leads to a slightly increased ($\times\sqrt{2}$) noise level [93, 94]. We have therefore chosen to correct our spectra S_g/S_e directly by calculating the correction term proportional to ϵ in Eq. (10) similar to Johns et al. [94] who obtained consistent results using either approach.

By defining the constant

$$C = \tau_w(1-\epsilon_w)B(T_c)D_d^2 \Big/ \left(B(T_s)D_s^2\right) \qquad (11)$$

and noting that $\tau + \epsilon = 1$, we obtain a quadratic equation in the gas transmittance:

$$C\tau^2 + (1-C)\tau - S_g/S_e = 0. \qquad (12)$$

This equation can be solved easily, also because the temperature of the absorption cell (T_c = 298 K) is much lower than the source temperature (T_s = 1620 K), which implies $C \ll 1$. The unique physical solution $\tau = 0.5\,C^{-1}\left(C - 1 + \sqrt{(1-C)^2 + 4CS_g/S_e}\right)$ of Eq. (12) can thus well be approximated by

$$\tau \simeq \frac{S_g}{S_e}\left[1 + \tau_w(1-\epsilon_w)\frac{B(T_c)D_d^2}{B(T_s)D_s^2}\left(1 - \frac{S_g}{S_e}\right)\right] \qquad (13)$$

Apparent measured transmittances S_g/S_e could therefore be converted into gas transmittances τ using the above equation, where Planck functions have been evaluated at measured cell temperatures (T_c around 298 K)

and our source temperature $T_s = 1620\,\mathrm{K}$. τ_w and $1-\epsilon_w$ have been calculated from known IR properties of BaF_2, which has been used as a window material for the 10 µm measurements. Because the window emissivity equals to its absorbance $\epsilon_w = \alpha_w$, it can be derived from the window thickness l, the window surface reflection coefficient R_w and the absorption coefficient β_w which has been determined by Deutsch [95]. It is well represented by an exponential in wavenumber $\beta_w(\nu) = 49641\,\mathrm{cm}^{-1}\exp(-\nu\,\mathrm{cm}/75.9)$ over the $800\,\mathrm{cm}^{-1}$ to $1250\,\mathrm{cm}^{-1}$ spectral range [96]. The reflection coefficient $R_w = (n-1)^2/(n+1)^2$ of BaF_2 for perpendicular incidence is calculated from the index of refraction n that can be represented in closed form by a Sellmeier equation over the 265 nm to 10.35 µm range [97]. Taking into account multiple reflections at both window interfaces, the window transmittance is given by [95]

$$\tau_w = \frac{(1-R_w)^2\exp(-\beta_w l)}{1-R_w^2\exp(-2\beta_w l)}, \tag{14}$$

where constants are as previously defined. Similarly, the absorbance can be calculated to yield

$$\alpha_w = \epsilon_w = \frac{(1-R_w)\,(1-\exp(-\beta_w l))\,(1+R_w\exp(-\beta_w l))}{1-R_w^2\exp(-2\beta_w l)} \tag{15}$$

In the ozone ν_1/ν_3 band region between $997\,\mathrm{cm}^{-1}$ and $1134\,\mathrm{cm}^{-1}$ the transmittance of our 4 mm window varies between 90.9% and 93.6%, whereas $(1-\epsilon_w)$ augments from 96.2% to 99.4% over the same wavenumber interval. We have compared overall transmittances obtained through Eq. (14) with measured transmittances of 4 and 5 mm windows provided by some manufacturers and with the 10% transmission value of a 32 mm thick window of the manufacturer who supplied our BaF_2 windows (Korth Kristalle GmbH, Germany). The agreement is within 0.01 and much better at 11.8 µm for the thick window.

According to Eq. (13), the relative error on the transmittance by not correcting the spectra is

$$u_r(\tau) = \frac{\Delta\tau}{\tau} \simeq (1-\tau)\tau_w(1-\epsilon_w)\frac{B(T_c)D_d^2}{B(T_s)D_s^2}, \tag{16}$$

where we have neglected the small difference between the gas transmittance and the ratio of measured spectra for the moment. For small absorptions ($\tau \sim 1$), the relative error vanishes and it never exceeds the ratio of Planck curves of the cell over the light source weighted by the ratio of the interferometer's exit over entrance areas, even for a non reflecting and perfectly transmitting window ($\tau_w(1-\epsilon_w) = 1$). Consequently, the related absolute uncertainty of the line intensity S which is proportional to the relative uncertainty in the transmittance disappears in the case of weak absorptions and becomes maximal for strong lines. This is opposite to the relative uncertainty of S (due to thermal emission), which vanishes in the latter case and takes the value of the term C in Eq. (11) when absorptions become weak. At $997\,\mathrm{cm}^{-1}$, C equals to $12.8\cdot10^{-3}$, and it diminishes towards higher wavenumbers ($8.5\cdot10^{-3}$ at $1134\,\mathrm{cm}^{-1}$). The strong wavenumber dependance also justifies why spectra have only been corrected in the 10 µm window. At $2000\,\mathrm{cm}^{-1}$, the ratio of Planck functions is only about $3\cdot10^{-4}$ and spectra at 5 µm were therefore left uncorrected.

In the above discussion (see equations (14) and (15)), we have assumed the absorption cell's window plates to have parallel faces, even though they are slightly wedged at 0.75°. Without multiple reflections, the term $\tau_w(1-\epsilon_w)$ becomes 0.887 at $1066\,\mathrm{cm}^{-1}$ instead of 0.914 in our approximation. The $\sim 2\%\ldots3\%$ difference is negligible compared to the relative uncertainty of the transmittance correction that we derive from assuming a triangular distribution function with limits between 0 (no correction) and $2C$ (twice the calculated value). Eq. (16) can be used to derive the associated uncertainty on the gas transmittance τ. This yields a thermal emission related standard uncertainty $u_{r,te}(\tau) = 6^{-1/2}C\,(1-\tau)$ or $4.3\cdot10^{-3}\,(1-\tau)$ at the centre $\nu = 1066\,\mathrm{cm}^{-1}$ of the analyzed spectral domain. This relative uncertainty itself depends on the transmittance of the ozone sample.

3.8. Uncertainty budget

The standard uncertainty of the line position determination has been discussed before (see Sec. 3.1) and is $u(\nu) = 3\cdot10^{-5}\,\mathrm{cm}^{-1}$ for all transitions of the ozone main isotopologue determined in this work. The full uncertainty budget of intensities of individual absorption lines depends on several contributions derived earlier (Sec. 3) and is obtained from the determining equation for the observed gas transmittance [13, 98]

$$\widetilde{\tau}_{IR}(\nu) = f_{app}(\nu) \otimes \exp\left[-n\left({}^{16}O_3\right) L_{IR}\, S\, g(\nu-\nu_0)\right], \tag{17}$$

which results from convolving the instrument function f_{app} with the transmittance at infinite resolution that is given by the Beer-Lambert law and depending on the ozone column density $n\left({}^{16}O_3\right)L_{IR}$, the line strength S and the molecular line profile $g(\nu-\nu_0)$ with line centre ν_0 of the transition. While both the column density $n\left({}^{16}O_3\right)L_{IR}$ and the line intensity S enter as numerical constants, the wavenumber dependent information

is determined by the normalized line profile and the apparatus function. Eq. (17) cannot be solved analytically to provide S as a function of measurands. The combined uncertainty of S must thus be derived differently than from the regular approach laid out in GUM [32]. The standard procedure to determine line strengths is to model the molecular absorption $S(T)g(\nu - \nu_0, p, T)$ as a function of temperature and the composition of the gas and use a numeric fitting routine to achieve best agreement between measured and calculated transmittances. Like Flores et al. [80], we use the numerical fitting approach to determine the sensitivity of the line intensity on the different quantities, such as the measured transmittance $\widetilde{\tau}_{IR}$, the line profile $g(\nu - \nu_0)$, the apparatus function $f_{app}(\nu)$ and the total ozone column $n\left(^{16}\mathrm{O}_3\right)L_{IR}$. We also assume that the different uncertainty components are uncorrelated, except for an evident correlation between $f_{app}(\nu)$ and $g(\nu - \nu_0)$ due to our instrument response being determined assuming a particular line profile function (see Paper II for more details). This correlation is taken into account in the sensitivity analysis by redetermining $f_{app}(\nu)$ whenever a parameter of the molecular line profile is changed.

The combined relative standard uncertainty of the line intensity $u_{c,r}(S)$ is then given by the square root of

$$u^2_{c,r}(S) = \sum_i c_i^2 u^2_{r,i}, \tag{18}$$

where the summation runs over the three independent factors ($f_{app}(\nu)$ & $g(\nu - \nu_0)$, $\widetilde{\tau}_{IR}$, $n\left(^{16}\mathrm{O}_3\right)L_{IR}$), with c_i being the individual sensitivity coefficients. Note that separation into sensitivity coefficient and standard uncertainty of the different contributions as given in Eq. (18) is not always meaningful, but is attempted whenever possible.

A final contribution to the uncertainty comes from rescaling intensities to the value at the reference temperature of 296 K, which is 2 K lower than our measurement conditions. This scaling is integrated into the spectral fitting routine [99], but can be considered separately, because it depends on independently measured quantities. Writing $S(T_{ref}) = S(T) \cdot F(T, T_{ref})$, it is given by [100]

$$F(T, T_{ref}) = \frac{Q(T)}{Q(T_{ref})} \frac{1 - e^{-c_2\nu/T_{ref}}}{1 - e^{-c_2\nu/T}} \frac{e^{-c_2E/T_{ref}}}{e^{-c_2E/T}} \tag{19}$$

where the factor $F(T, T_{ref})$ describes the intensity change due to changing the thermal population of energy levels by adjusting the temperature from T to T_{ref}. Here, $T \simeq 298$ K is the measurement temperature, $T_{ref} = 296$ K the reference temperature of the database, $c_2 = 1.438776877$ cm K the second radiation constant, Q the total internal partition sum (TIPS) or function of the molecule ($^{16}\mathrm{O}_3$) and ν and E the transition and lower state energies in units of cm^{-1}, respectively. It is apparent from Eq. (19) that the relative uncertainty of $S(T_{ref})$ must be obtained as a (quadratic) sum of relative uncertainties of both, $S(T)$ and $F(T, T_{ref})$.

Before quantifying the different uncertainty contributions, we recall the typical measurement conditions in Table 7, where the observed ranges and representative values are summarized. To keep the analysis as simple as possible, we restrict ourselves on deriving uncertainties for all lines in the 5 µm region and for the strongest lines (80% of all lines) covering one decade of line intensities ($S \geq 4 \cdot 10^{-21}$ cm molecule^{-1}) in the 10 µm region. In this way, the uncertainty budget can be derived using representative values that characterize a relatively homogeneous group of data.

3.8.1. Ozone column

The uncertainty budget for the ozone columns $n(^{16}\mathrm{O}_3)L_{\mathrm{IR}}$ is presented in Table 8. Length and number density measurements are completely independent for the long cell arm and thus for the measurements in the 5 µm region. The very slight correlation in the short paths has been neglected, because the uncertainty of the IR path length is largely dominated by the presence of multiple reflections rather than the measurement of the cell length itself (see Sec. 3.2.1). What is more, any cell length bias leads to the same negative bias in the number density. It thus cancels when the column in the short path is calculated and the current estimation is thus rather conservative. Two independent factors then enter in the determination of $n(^{16}\mathrm{O}_3)$: the uncertainty of the $^{16}\mathrm{O}_3$ mole fraction derived in Sec. 3.6.2 and the number density of ozone. The latter depends on the UV absorbance, the UV absorption cross section and the UV cell length via $n(\mathrm{O}_3) = A_{UV}/(\sigma_{UV}L_{UV})$, such that its relative uncertainty can be obtained as the square root of the quadratic sum of the relative uncertainties of these three independent measurands given in Sec. 3.3. As shown in Table 8, the relative standard uncertainty of the ozone column $u_r\left(n(^{16}\mathrm{O}_3)L_{\mathrm{IR}}\right)$ is $6.1 \cdot 10^{-3}$ (5 µm) or $7.8 \cdot 10^{-3}$ (10 µm), depending on the wavelength range. It is mostly determined by the path length uncertainties in the IR and the uncertainty of the UV absorption cross section.

The corresponding sensitivity coefficient (see Eq. (18)) is $c\left(n(^{16}\mathrm{O}_3)L_{IR}\right) = -1$ and the quadratic uncertainty contribution terms $c^2\left(n(^{16}\mathrm{O}_3)L_{IR}\right)u_r^2\left(n(^{16}\mathrm{O}_3)L_{IR}\right)$ are $6.1 \cdot 10^{-5}$ for

Table 7: Experimental conditions. Peak absorbances are indicative values given for infinite measurement resolution and assuming a simple Doppler profile. Representative values have been determined as means from the two extremes of the observed range, with the representative sample pressure and peak absorbances being geometric means of the two boundary values. The range of peak absorbances was further reduced by taking the largest pressure for calculating the absorption of the weakest lines and the lowest pressure for absorbances of the strongest lines and comprises intensities within one decade only.

No	Parameter, Symbol / Unit	Parameter range	Representative value
1	Ozone pressure, $p(O_3)$ / hPa	0.19 – 1.52	0.54
2	Temperature, T / K	297.6 – 298.4	298.0
3	Line position (5 µm), ν_0 / cm^{-1}	2066 – 2132	2099
4	Line position (10 µm), ν_0 / cm^{-1}	997 – 1134	1066
5	Line intensity (5 µm), S / cm molecule^{-1}	$5.2 \cdot 10^{-22}$ – $3.8 \cdot 10^{-21}$	–
6	Line intensity (10 µm), S / cm molecule^{-1}	$9.3 \cdot 10^{-22}$ – $4.2 \cdot 10^{-20}$	–
7	Peak absorbance (5 µm), A_{pk} / 1	0.086 – 0.63	0.23
8	Peak absorbance (10 µm),[a] A_{pk} / 1	0.36 – 0.75	0.52

[a] At 10 µm the range has been restricted to lines from the decade with $S \geq 4 \cdot 10^{-21}$ cm molecule^{-1}. This corresponds to more than 80% of the measured transitions.

Table 8: Uncertainty budget for the absorption columns of the ozone main isotopologue.

No.	Quantity, Symbol / Unit	Typical or reference value	Rel. standard uncertainty u_r
1.	Particle number density of $^{16}O_3$, $n(^{16}O_3)$ / cm^{-3}	$1.23 \cdot 10^{16}$	$4.0 \cdot 10^{-3}$
1.1	Fraction of $^{16}O_3$, $r(666)$ / 1	0.9929	$2.0 \cdot 10^{-4}$
1.2	Ozone number density, $n(O_3)$ / cm^{-3}	$1.24 \cdot 10^{16}$	$3.9 \cdot 10^{-3}$
1.2.1	Length of UV path, L_{UV} / mm	50.961	$1.4 \cdot 10^{-3}$
1.2.2	O_3 absorption cross section, σ_{UV} / cm^2	$1.1329 \cdot 10^{-17}$	$3.1 \cdot 10^{-3}$
1.2.3	UV absorbance, A_{UV} / 1	2.05	$2.0 \cdot 10^{-3}$
2.	Length of long IR path, $L_{IR,l}$ / mm	200.50	$4.7 \cdot 10^{-3}$
	Length of short IR path, $L_{IR,s}$ / mm	51.06	$6.7 \cdot 10^{-3}$
Column density of $^{16}O_3$ at 5 µm, $n(^{16}O_3)L_{IR,l}$ / cm^{-2}		$2.5 \cdot 10^{17}$	$6.1 \cdot 10^{-3}$
Column density of $^{16}O_3$ at 10 µm, $n(^{16}O_3)L_{IR,s}$ / cm^{-2}		$6.1 \cdot 10^{16}$	$7.8 \cdot 10^{-3}$

the 10 µm region and $3.7 \cdot 10^{-5}$ for the 5 µm region, respectively.

3.8.2. *Apparatus function and molecular line profile*

Eq. (17) indicates that the choice of the instrument line shape (ILS) f_{app} and the molecular line profile alike have an impact on the intensity measurement. Because the same spectra are used to determine the instrumental line shape and to measure the line intensities and also because LINEFIT [101] requires the molecular profile as an input for calculating the ILS (see Paper II), the two determinations are necessarily dependent and must be treated consistently. In the second paper of the series, we have therefore not only studied in as much the ILS varies as a function of spectrum, pressure or microwindow, thus how well the ILS can be determined assuming that the molecular line profile is known. We have also investigated the impact of choosing different molecular line parameters on the apparatus function and the intensity measurements.

Figure 5 of Paper II indicates that even at 10 µm, changing the self broadening parameter γ_0 by ±5.0% which must be regarded a typical value [102] and roughly corresponds to the 1-σ uncertainty estimate from the uncertainty limit of better than 10% indicated in HITRAN 2016, leads to intensity changes within ±0.29%. Assuming a rectangular distribution within this margin, we obtain a relative standard uncertainty of 0.17%. At 5 µm, the impact is only one third that value. The impact of using either a qSDVP or the Voigt profile is less than about 0.10% at 5 µm, corresponding to an uncertainty of 0.58 ‰. The effect on line intensities at 10 µm is more pronounced, however (see Fig. 6 in Paper II). But even for a quadratic coefficient in the upper range of typical values of $\gamma_2 = 0.15\gamma_0$ (see [103] for CO_2, for example), intensities of lines belonging to the decade of highest intensities remain within +1.1 ‰ and –4.4 ‰. Again assuming a rectan-

gular probability distribution, a relative uncertainty of 2.5 ‰ (= 4.4/ $\sqrt{3}$ ‰) is obtained. The repeatability of f_{app} has been assessed by comparing different ozone spectra (see Fig. 3 and Table 3 of Paper II) and the adequacy of the line shape model was roughly investigated through comparison with the analytic expression (Eqs. (1) and (2) in Paper II). Intensities remained within +2.6 ‰ and −1.7 ‰ at 5 µm and between +1.6 ‰ and −4.5 ‰ at 10 µm when using a single spectrum for the determination of f_{app}. Since high pressure spectra provided the best absorption-to-noise ratio, we analyze the scatter in the LINEFIT ILS derived from spectra 1, 2, 5 and 6. From these, the most reliable f_{app} had been constructed as an average. Relative standard uncertainties of the averaged ILS of 0.71 ‰ and 1.1 ‰ have thus been obtained for 5 µm and 10 µm, respectively. As discussed in Paper II, the scatter of ILS parameters or intensities resulting from ILS derived from individual spectra corresponds to the dispersion of the same numbers when using different micro-windows on the same spectra. By comparing the ILS with its analytical form for two entrance aperture radii which correspond to the nominal (R = 0.575 mm) and the measured (R = 0.545 mm) value, we try to give a conservative estimate for the accuracy of the ILS model, i.e. approximate how well the LINEFIT derived ILS reproduces the instrumental apparatus function. Strictly speaking, only the inverse is feasible: estimating the accuracy of the ideal ILS by comparison with the much more realistic ILS derived by LINEFIT. The validity of the latter is demonstrated by the capability of removing the residuals that remain when using the ideal ILS (see Fig. 1 of Paper II). The application and development of more sophisticated methods such as using tunable narrow lasers to determine the ILS unambiguously would be beyond the scope of the current paper, however. We therefore use the maximum deviation between the two ILS models as a proxy for the trueness of the LINEFIT ILS. These deviations are 7.9 ‰ at 5 µm and −4.8 ‰ at 10 µm. With these very conservative margins, we assume a triangular probability distribution and obtain relative standard uncertainties of 3.2 ‰ and 2.0 ‰ for the two spectral regions, respectively.

Due to our crude estimate of the trueness of the ILS, this contribution is dominant at 5 µm, because spectral residuals in this region show a more pronounced asymmetry than at 10 µm, leading to a more significant departure between ideal and real ILS. This does not necessarily imply that the ILS there is more inaccurate. We believe that the opposite is the case, but just have no better means to estimate this particular uncertainty component. At 10 µm, where the ILS is closer to the ideal form, uncertainties in the molecular line profile and the pressure parameters dominate the relative uncertainty of the uncertainty component related to the instrument line shape and the molecular profile. As shown in Table 9 which lists indiidual uncertainty contributions due to the apparatus function and the molecular line profile, the overall quadratic contributions to the uncertainty budget $\left(c(f_{app}\&g(\nu-\nu_0))\,u_r(f_{app}\&g(\nu-\nu_0))\right)^2$ respectively are $1.2\cdot10^{-5}$ and $1.4\cdot10^{-5}$ in the two regions.

3.8.3. Transmittance measurement

The different quantities, their uncertainties and their contribution to the relative uncertainty of the line intensity measurement are listed in Table 10. The weak thermal emission at 5 µm has been neglected. This yields $c^2(\tau)u_r^2(\tau) = 3.5\cdot10^{-5}$ at 10 µm and $c^2(\tau)u_r^2(\tau) = 2.2\cdot10^{-5}$ at 5 µm.

3.8.4. Intensity scaling

Measured intensities have been scaled to the 296 K reference temperature, implying that the relative uncertainty of the intensity scaling factor F needs to be determined. It can be determined from Eq. (19) using standard propagation rules:

$$u_r^2(F) = F^{-2}\sum_i\left(\frac{\partial F}{\partial x_i}\right)^2 u^2(x_i), \qquad (20)$$

where the x_i run over the independent measurands ν, E, Q and T in Eq. (19). As before, we evaluate the different uncertainty contributions in Eq. (20) numerically by evaluating the change of F due to a change in x_i of $\pm u(x_i)$ [32]. Uncertainties in ν and E don't contribute significantly. Transition energies ν enter into Eq. (19) only in terms of multiplicative factors of the form $(1-\exp(-c_2\nu/T_{ref}))\,/\,(1-\exp(-c_2\nu/T))$. Even for the lowest transition energy of 997 cm^{-1} in our study, relative changes of these terms remain at the $1.2\cdot10^{-9}$ level when ν changes by $u(\nu) = 3\cdot10^{-5}$ cm^{-1}, the standard uncertainty of the transition energy. This contribution can be safely neglected, as well as contributions from the lower state energy terms E. We assume uncertainties of these energies to be $u(E) = 0.001$ cm^{-1}, the upper limit of uncertainties given for ozone line positions in HITRAN. This leads to a relative uncertainty contribution $\exp(-c_2u(E)/298\,\mathrm{K})\,/\exp(-c_2u(E)/296\,\mathrm{K}) - 1 = 3.3\cdot10^{-8}$. Ozone TIPS are assumed to be accurate at the percent level or better [104], but the ratio of partition functions at similar temperatures is known with much higher accuracy. Gamache et al. [104], for example, report $Q(296\,K) = 3483.7$, which is 0.3%

Table 9: Impact of the molecular line profile and the apparatus function on the uncertainty of the line intensity

No	Quantity, Symbol / Unit	Rel. standard uncertainty u_r	Unc. contribution	
			5 µm	10 µm
1.	Average pressure broadening, γ_0 / cm^{-1}	$5.0 \cdot 10^{-2}$	$5.8 \cdot 10^{-4}$	$1.7 \cdot 10^{-3}$
2.	qSDVP model, $g(\nu - \nu_0)$ / 1	–	$5.8 \cdot 10^{-4}$	$2.9 \cdot 10^{-3}$
3.	ILS repeatability, f_{app} / 1	–	$1.1 \cdot 10^{-3}$	$7.1 \cdot 10^{-4}$
4.	Trueness of ILS, f_{app} / 1	–	$3.2 \cdot 10^{-3}$	$2.0 \cdot 10^{-3}$
Profile and ILS related relative uncertainty of line intensity			$3.5 \cdot 10^{-3}$	$3.7 \cdot 10^{-3}$

Table 10: Impact of IR transmittance uncertainties on the uncertainty of the line intensity. The asterisk (*) gives estimation after the signal has been corrected using the software routine provided by the FTS manufacturer (see Section 3.7.2)

No.	Quantity, Symbol / Unit	Typical value	Rel. standard uncertainty u_r	Contribution to rel. unc.
1.	Spectral noise of transmittance at 5 µm, τ / 1	0.85	$5.6 \cdot 10^{-4}$	$2.9 \cdot 10^{-3}$
	Spectral noise of transmittance at 10 µm, τ / 1	0.63	$1.7 \cdot 10^{-3}$	$4.7 \cdot 10^{-3}$
2.	Detector non-linearity at 5 µm, τ / 1	0.85	$5.8 \cdot 10^{-4}$	$3.6 \cdot 10^{-3}$
	Detector non-linearity* at 10 µm, τ / 1	0.63	$5.8 \cdot 10^{-4}$	$1.2 \cdot 10^{-3}$
3.	Thermal emission at 5 µm, τ / 1	0.85	$1.5 \cdot 10^{-4}$	–
	Thermal emission at 10 µm, τ / 1	0.63	$4.3 \cdot 10^{-3}(1 - \tau)$	$3.4 \cdot 10^{-3}$
Transmittance related relative uncertainty of line intensity at 5 µm				$4.6 \cdot 10^{-3}$
Transmittance related relative uncertainty of line intensity at 10 µm				$5.9 \cdot 10^{-3}$

larger than the value given by the S&MPO database ($Q(296\,K) = 3473.0$) in February 2021 [105]. However, the value $Q(298\,\mathrm{K})/Q(296\,\mathrm{K}) = 1.0113959$ is identical for both calculations within all significant digits. We can therefore conclude that the relative uncertainty $u_r\,(Q(298\,\mathrm{K})/Q(296\,\mathrm{K}))$ is smaller than 10^{-4} and can be ignored.

The dominant uncertainty contribution to the scaling factor comes from the temperature uncertainty of the measurement. The temperature sensitivity of F in Eq. (19) strongly depends on the lower state energy. The highest lower state energy in our study is 1101.741 cm^{-1}. For this value, F varies by $\mp 3.1 \cdot 10^{-3}$ relative, when T is varied by the standard uncertainty of our temperature measurement $u(T) = \pm 0.26$ K. For the lower state energy of 0 cm^{-1}, the relative variation of F is dominated by changes in the partition function, which is $\pm 1.5 \cdot 10^{-3}$. For an arbitrary transition, F will thus vary within $\mp 3.1 \cdot 10^{-3}$ and, assuming a rectangular probability distribution function, we obtain the relative standard uncertainty of $u_r(F) = 1.8 \cdot 10^{-3}$. Indeed, for all transitions with lower state energies smaller than 785 cm^{-1}, relative intensity changes remain within $\pm 1.8 \cdot 10^{-3}$, almost independent of the transition energy ν. This corresponds to all transitions in the 5 µm region, where the highest lower state energy is 676.796 cm^{-1} and to 471 ($\sim$ 95%) out of 497 transitions at 10 µm, including all transitions with intensities $\geq 4 \cdot 10^{-21}$ cm molecule^{-1} in this region.

3.8.5. Combined uncertainty

The different contributions from Secs. 3.8.1–3.8.4 determine the combined standard uncertainty of the line intensities. Table 11 gives the summary budget and shows that uncertainties related to the absorption length have the strongest impact on the accuracy of the determination of individual line intensities, but that other factors except for the intensity scaling contribute considerably. Nevertheless, details of the molecular line profile or testing the adequacy of the instrument line shape (see Section 3.8.2) are relatively minor issues in the present study, as these uncertainties contribute only about 10% to the overall budget. The combined relative standard uncertainty of the line strength of a single isolated line of ozone is $u_r(S) = 1.1 \cdot 10^{-2}$ at 10 µm and $u_r(S) = 8.6 \cdot 10^{-3}$ at 5 µm after rescaling to the reference temperature. Taking the larger of these two values, we can assign a relative standard uncertainty of $u_r(S) = 1.1 \cdot 10^{-2}$ to all of our intensity measurements. To our knowledge, this is the first measurement at the one-percent accuracy level, in both the fundamental band region at 10 µm as well as in the overtone or combination band region at 5 µm.

Table 11: Uncertainty budget for $^{16}O_3$ line intensity measurements. The uncertainty for a line intensity measurement is determined by the sum of three major contributions (nos. 1 to 3). A fourth contribution needs to be added when scaling the line intensity to the reference temperature.

No	Quantity, Symbol	Squared contribution $c_i^2 u_{r,i}^2$		Combined rel. standard uncertainty $u_{c,r}$	
		5 µm	10 µm	5 µm	10 µm
1.	Column density of $^{16}O_3$, $n(^{16}O_3)\,L_{IR}$	$3.7 \cdot 10^{-5}$	$6.1 \cdot 10^{-5}$	–	–
2.	ILS & molecular profile, f_{app} & $g(\nu - \nu_0)$	$1.2 \cdot 10^{-5}$	$1.4 \cdot 10^{-5}$	–	–
3.	Infrared transmittance, τ	$2.2 \cdot 10^{-5}$	$3.5 \cdot 10^{-5}$	–	–
Measured line intensity, $S(T)$		$7.0 \cdot 10^{-5}$	$11.0 \cdot 10^{-5}$	$8.4 \cdot 10^{-3}$	$10.5 \cdot 10^{-3}$
4.	Intensity scaling, F	$3.2 \cdot 10^{-6}$		–	–
Line intensity, $S(T_{ref})$		$7.3 \cdot 10^{-5}$	$11.3 \cdot 10^{-5}$	$8.6 \cdot 10^{-3}$	$10.6 \cdot 10^{-3}$

4. Discussion and conclusion

We have presented a new experiment for the quasi simultaneous measurement of ozone spectroscopic data in both the 5 µm and 10 µm regions. These measurements are based on a newly developed double path absorption cell that could be integrated in a commercial high-resolution Michelson interferometer. Six ozone measurements at low pressure (between 0.2 hPa and 1.5 hPa) with very little ozone decomposition have been performed and the instantaneous ozone partial pressures were measured in the UV using the newly recommended ozone absorption cross section at 253.65 nm [18]. Care has been taken to minimize systematic biases and a comprehensive uncertainty budget has been presented. The analysis shows that line positions could be determined with a standard uncertainty of $u(\nu_0) = 3.0 \cdot 10^{-5}\,\mathrm{cm}^{-1}$. The intensities of the measured lines with $S \geq 4 \cdot 10^{-21}\,\mathrm{cm\,molecule}^{-1}$ (80% of 497 transitions) in the 10 µm region and of all lines in the 5 µm region have been determined with a relative standard uncertainty of $u_r(S) = 1.1 \cdot 10^{-2}$ or better. This is the first time that a one-percent intensity uncertainty is demonstrated for ozone transitions in the mid-infrared. The fact that the accurate data from two spectral bands (at 5 µm and at 10 µm) have been obtained from the same sample and have undergone identical analysis provides a homogenous data set of particular interest for comparison with molecular calculations. While the detailed presentation of the data is subject of the second paper of this series [34], it should be pointed out that the random errors due to signal noise lead to a typical intensity uncertainty of 0.5%. This is consistent with the level of fluctuation that is observed in line by line comparisons with very recent data and new molecular calculations that are presented in Paper II. Most of the uncertainties discussed here enter systematically in the budget of an individual line such that all lines are affected in the same manner. This concerns uncertainties related to the ozone column determination (see Sec. 3.8.1) or the thermal correction, for example. Other uncertainty components, such as the signal noise are completely uncorrelated from one line to another, but there are sources where such a clear distinction is not possible, such as the uncertainty due to biases in the broadening parameter. In order to provide an idea in as much individual line measurements can provide independent information, we specify the range for the correlated and uncorrelated uncertainty components from two limiting assumptions. In the first case, we only consider spectral noise as an uncorrelated source, in the second only uncertainties concerning the column density, the thermal correction and the ILS are considered completely correlated. At 5 µm, this yields a range of (7.0...8.1) ‰ and (2.9...5.0) ‰ for the correlated and uncorrelated relative standard uncertainties, respectively. The corresponding ranges in the 10 µm region are (9.3...9.9) ‰ and (4.7...5.1) ‰. Focussing on the 10 µm data for the moment, we conclude that uncorrelated relative standard uncertainties are about 5 ‰.

The high accuracy of the present data will help to resolve the discrepancy observed in atmospheric ozone retrievals using UV as compared to mid-infrared spectroscopic data. It will also allow to verify or correct line intensities in the HITRAN 2016 database, which are believed to suffer from a bias between 2% and 4%. It must be stressed that the current data set and the presented analysis are original and entirely independent from any other mid-infrared data published so far. It makes use of the most recent recommendations for the calibration of the amount of ozone measurement.

Acknowledgement

The authors would like to thank two anonymous reviewers for their helpful comments. We also thank the

entire technical staff at LERMA for their help and Sorbonne Université for the funding of the FTS-Paris instrument. This work was supported by the French national program LEFE/INSU.

Appendix A. Effective path length for an inclined and divergent light beam

A conical beam with divergence angle $0 \leq \alpha \leq \alpha_m$ hits the window of an optical cell at a distance x from the focal point (the analysis for a convergent beam is analogous). We assume a radial intensity profile, only depending on the distance from the central propagation axis and without azimuthal dependence $0 \leq \phi < 2\pi$. If the window is perpendicular to the centre beam, different beam pencils will have lengths between l and $l\sec(\alpha_m)$, leading to an augmentation of the average beam length. Assuming the distance to the focal point being l, we get for the focal distance of a particular beam pencil

$$s(\phi, \alpha, \theta) = \frac{l\sec(\alpha)}{1 - \cos(\phi)\tan(\theta)\tan(\alpha)}, \qquad \text{(A.1)}$$

where θ is the inclination angle between the beam centre and the window normal. We adopt the convention that the beam propagates horizontally (along the x-axis) and that the window is inclined by turning the vertical (z) axis around the y-axis (see Fig. A.4 for illustration of the geometry and parameters ϕ, α, θ). Using Eq. (A.1)

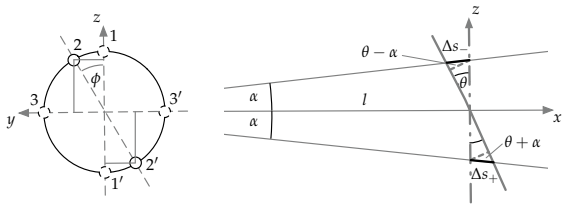

Figure A.4: Illustration of effect of window tilt on path length prolongation in a divergent beam. *Left* : view on the non-tilted window along the beam propagation (x-axis). The choice of coordinate system (x, y, z) is indicated by arrows. Three points (corresponding to a fixed divergence angle α are shown (1 on vertical axis ($\phi = 0$), 2 ($0 < \phi \leq \pi/2$), 3 on the horizontal (y) axis ($\phi = \pi/2$)). Primed coordinates correspond to points reflected at origin ($\phi' = \phi + \pi$). *Right* : side view of beam cone impinging on window. Un-inclined window is shown as dashed vertical line, the inclined window as a solid line. Bold dark lines indicate changes of the beam pencil length ($\Delta s_+, \Delta s_-$) for a pair (ϕ, ϕ') as compared to the vertical ($\theta = 0$) window. Dashed grey perpendiculars illustrate that corrections for ϕ and $\phi' = \phi + \pi$ to first order cancel each other.

alone, we can show that window inclination leads to an effect that is only fourth order in angles (α and θ). If we calculate s for a beam pencil ($\phi = \phi_0$) and its complement ($\phi = \phi_0 + \pi$) and compare it to the corresponding value for the non-inclined window,

$$\begin{aligned}\frac{1}{2}\left(\frac{\Delta s(\phi)}{s} + \frac{\Delta s(\phi+\pi)}{s}\right) &= \frac{\Delta s_+ + \Delta s_-}{2s} \\ &= \left(1 - \cot^2(\alpha)\cot^2(\theta)\sec^2(\phi)\right)^{-1} - 1 \qquad \text{(A.2)} \\ &\simeq \cos^2(\phi)\,\alpha^2\theta^2 + \ldots, \qquad \text{(A.3)}\end{aligned}$$

we find that the relative path change is majored by $\alpha_m^2\theta^2$. Note that Eq. (A.3) implies that the $\alpha_m^2\theta^2$ term has a prefactor < 1 due to the contribution of beam pencils with $\alpha < \alpha_m$ and $\cos^2(\phi) < 1$.

For $\theta = 0$, we obtain an exact analytic expression for the effective path length due to beam divergence by averaging the focal point distance $s(\alpha) = l\sec(\alpha)$ over the radial intensity distribution, which is best described by assuming that an original collimated beam with homogeneous intensity is focussed onto a point, thus $I(r) \sim r \Rightarrow I(\alpha) \sim \tan(\alpha)$:

$$\begin{aligned}\overline{s}(\theta = 0) &= \int_0^{\alpha_m} I(\alpha)s(\alpha,\theta)\,d\alpha \Big/ \int_0^{\alpha_m} I(\alpha)\,d\alpha \\ &= \frac{2}{3}l\cot^2(\alpha_m)\left[\sec^3(\alpha_m) - 1\right] \qquad \text{(A.4)}\end{aligned}$$

We need to replace l by $d\sec(\theta)$ in Eq. (A.4) for obtaining the path length between the two cell windows. This finally leads to the small angle approximation for the effective length L of the divergent beam in the cell

$$L = \frac{2d}{3}\cot^2(\alpha_m)\left[\sec^3(\alpha_m) - 1\right]\sec(\theta). \qquad \text{(A.5)}$$

This expression is correct to quadratic (and even third-order) terms in α_m and θ, provided that the beam possesses azimuthal symmetry and a radially varying intensity profile $I(r) \sim r = \sqrt{y^2 + z^2}$. It becomes inappropriate when forth order terms cannot be neglected.

Appendix B. Oxygen isotopes and delta notation

The isotopic composition of a substance can be described by the comparison with respect to an international standard substance, which in case of oxygen commonly is VSMOW (Vienna Standard Mean Ocean Water) [106]. Its composition is given by $R^{18} = (2005.20 \pm 0.43) \cdot 10^{-6}$ [107] and $R^{17} = (379.9 \pm 1.6) \cdot 10^{-6}$ [108], where $R^i = N(^i\mathrm{O})/N(^{16}\mathrm{O})$ denotes the isotope abundance ratio of the rare isotope ^{i}O ($i = 17, 18$) with respect to the main isotope. Deviations from the reference

isotopic composition are reported using the δ-notation

$$\delta^i = \frac{R^i}{R^i_{\mathrm{VSMOW}}} - 1, \tag{B.1}$$

which usually is given in units of ‰. If we denote by $r^i = N(^i\mathrm{O})/(N(^{16}\mathrm{O}) + N(^{17}\mathrm{O}) + N(^{18}\mathrm{O}))$ the fraction of the ^{i}O isotope, we can calculate the relative abundance of the main ozone isotopologue $r_{666} = \left(r^{16}\right)^3$ using combinatorial rules

$$r_{666} = \left(1 + R^{18}_{\mathrm{VSMOW}}\left(1 + \delta^{18}\right) + R^{17}_{\mathrm{VSMOW}}\left(1 + \delta^{17}\right)\right)^{-3} \tag{9}$$

and eventual departures from the statistical distribution can be safely ignored for the main isotopologue. The relative uncertainty of r_{666} can be immediately calculated and simplifies to

$$\begin{aligned}\frac{u^2_r\left(r_{666}\right)}{9} &= \left(1 + \delta^{18}\right)^2 u^2\left(R^{18}_{\mathrm{VSMOW}}\right) + \left(1 + \delta^{17}\right)^2 u^2\left(R^{17}_{\mathrm{VSMOW}}\right) \\ &\quad + \left(R^{18}_{\mathrm{VSMOW}}\right)^2 u^2\left(\delta^{18}\right) + \left(R^{17}_{\mathrm{VSMOW}}\right)^2 u^2\left(\delta^{17}\right) \\ &\simeq \left(R^{18}_{\mathrm{VSMOW}}\right)^2 u^2\left(\delta^{18}\right)\end{aligned} \tag{B.2}$$

if we neglect a term that contributes to the uncertainty by less than 1%. In the last line of Eq. (B.2), we have just retained the dominant term in ^{18}O. Assuming similar uncertainties in δ^{17} and δ^{18}, this term has an about 25 times higher weight in the quadratic sum than the corresponding term in ^{17}O. Moreover, the squared uncertainties in R_{VSMOW} sum up to less than $2 \cdot 10^{-6}$. Since $u(\delta)$ is larger than 10^{-2}, the retained term must contribute at least 100 times more than the $u(R_{\mathrm{VSMOW}})$ terms in the quadratic sum. Using the values finally derived in Sec. 3.6.2, we note that the approximation given in the last line of Eq. (B.2) differs from the full expression by less than 0.5% .

References

[1] World Meteorological Organization (WMO), Scientific assessment of ozone depletion: 2014, World Meteorological Organization, Global ozone research and monitoring project—report, Report No. 55, 2014.

[2] J. Viallon, P. Moussay, J. E. Norris, F. R. Guenther, R. I. Wielgosz, Metrologia 43 (2006) 441–50.

[3] J. M. Flaud, R. Bacis, Spectrochim. Acta A 54 (1998) 3–16.

[4] K. Mauersberger, D. Hanson, J. Barnes, J. Morton, J. Geophys. Res. 92 (1987) 8480–2.

[5] C. Claveau, C. Camy-Peyret, A. Valentin, J. M. Flaud, J. Molec. Spectrosc. 206 (2001) 115–25.

[6] M. R. DeBacker-Barilly, A. Barbe, J. Molec. Spectrosc. 205 (2001) 43–53.

[7] G. Wagner, M. Birk, F. Schreier, J. M. Flaud, J. Geophys. Res. 107 (2002) 4626.

[8] M. A. H. Smith, V. M. Devi, D. C. Benner, C. P. Rinsland, J. Geophys. Res. 106 (2001) 9909–21.

[9] B. Picquet-Varrault, J. Orphal, J.-F. Doussin, P. Carlier, J.-M. Flaud, J. Phys. Chem. A 109 (2005) 1008 –14.

[10] A. Gratien, B. Picquet-Varrault, J. Orphal, J. F. Doussin, J. M. Flaud, J. Phys. Chem. A 114 (2010) 10045–8.

[11] C. Viatte, M. Schneider, A. Redondas, F. Hase, M. Eremenko, P. Chelin, J. M. Flaud, T. Blumenstock, J. Orphal, Atmos. Meas. Tech. 4 (2011) 535–46.

[12] A. Kagawa, Y. Kasai, N. B. Jones, M. Yamamori, K. Seki, F. Murcray, Y. Murayama, K. Mizutani, T. Itabe, Atmos. Chem. Phys. 7 (2007) 3791–810.

[13] M. Guinet, D. Mondelain, C. Janssen, C. Camy-Peyret, J. Quant. Spectrosc. Radiat. Transfer 111 (2010) 961–72.

[14] X. Thomas, P. Von Der Heyden, M. R. De Backer-Barilly, M. T. Bourgeois, A. Barbe, J. Quant. Spectrosc. Radiat. Transfer 111 (2010) 1080–8.

[15] C. Janssen, C. Boursier, P. Jeseck, Y. Té, J. Mol. Spectrosc. 326 (2016) 48–59.

[16] B. J. Drouin, T. J. Crawford, S. Yu, J. Quant. Spectrosc. Radiat. Trans. 203 (2017) 282–92.

[17] M. Birk, G. Wagner, I. E. Gordon, B. Drouin, J. Quant. Spectrosc. Radiat. Transfer 226 (2019) 60–5.

[18] J. T. Hodges, J. Viallon, P. J. Brewer, B. J. Drouin, V. Gorshelev, C. Janssen, S. Lee, A. Possolo, M. A. H. Smith, J. Walden, R. Wielgosz, Metrologia 56 (2019) 034001.

[19] A. G. Hearn, Proc. Phys. Soc. 78 (1961) 932–40.

[20] A. M. Bass, R. J. Paur, The ultraviolet cross-sections of ozone: I. the measurements. In: C.S. Zerefos and A. Ghazi (eds) Atmospheric Ozone, Dordrecht, Springer Netherlands, 1985, pp. 606–10.

[21] R. J. Paur, A. M. Bass, The ultraviolet cross-sections of ozone: II. results and temperature dependence. In: C.S. Zerefos and A. Ghazi (eds) Atmospheric Ozone, Dordrecht, Springer Netherlands, 1985, pp. 611–6.

[22] V. Gorshelev, A. Serdyuchenko, M. Weber, W. Chehade, J. P. Burrows, Atmos. Meas. Tech. 7 (2014) 609–24.

[23] J. Malicet, D. Daumont, J. Charbonnier, C. Parisse, A. Chakir, J. Brion, J. Atmos. Chem. 21 (1995) 263–73.

[24] J. Orphal, J. Staehelin, J. Tamminen, G. Braathen, M. R. De Backer, A. F. Bais, D. Balis, A. Barbe, P. K. Bhartia, M. Birk, J. B. Burkholder, K. V. Chance, T. von Clarman, A. Cox, D. Degenstein, R. Evans, J. M. Flaud, D. Flittner, S. Godin-Beckmann, V. Gorshelev, E. Hare, C. Janssen, E. Kyrölä, T. McElroy, R. McPeters, M. Pastel, M. Petersen, I. Petropavlovskikh, B. Picquet-Varrault, M. Pitts, G. Labow, M. Rotger-Langerau, T. Leblanc, C. Lerot, X. Liu, P. Moussay, A. Redondas, M. Van Roozendael, S. P. Sander, M. Schneider, A. Serdyuchenko, P. Veefkind, J. Viallon, C. Viatte, G. Wagner, M. Weber, R. I. Wielgosz, C. Zahner, J. Mol. Spectrosc. 327 (2016) 105–21.

[25] M. Birk, Wagner, ESA SEOM-IAS – measurement and ACS database O_3 UV region (version ii), 2021. doi:10.5281/zenodo.1485587.

[26] N. Glatthor, T. von Clarmann, G. P. Stiller, M. Kiefer, A. Laeng, B. M. Dinelli, G. Wetzel, J. Orphal, Atmos. Meas. Tech. 11 (2018) 4707–32.

[27] M. Minissale, T. Zanon-Willette, P. Jeseck, C. Boursier, C. Janssen, J. Mol. Spectrosc. 348 (2018) 103 –13.

[28] V. Tyuterev, A. Barbe, D. Jacquemart, C. Janssen, S. Mikhailenko, E. Starikova, J. Chem. Phys. 150 (2019) 184303.

[29] A. Barbe, S. Mikhailenko, E. Starikova, V. Tyuterev, J. Quant. Spectrosc. Radiat. Transfer 276 (2021) 107936.

[30] V. Tyuterev, A. Barbe, S. Mikhailenko, E. Starikova,

Y. Babikov, J. Quant. Spectrosc. Radiat. Transfer 272 (2021) 107801.
[31] M. Birk, G. Wagner, A. Barbe, M.-R. De Backer, M. Rotger, ESA SEOM-IAS – measurement and line parameter database O_3 MIR region (version ii), 2021.
[32] JCGM-WG1 2008 Working Group, Evaluation of measurement data – Guide to the expression of uncertainty in measurement, Technical Report JCGM 100:2008, BIPM, IEC, IFCC, ILAC, ISO, IUPAC, IUPAP and OIML, 2008.
[33] I. E. Gordon, L. S. Rothman, et al., J. Quant. Spectrosc. Radiat. Transfer (2021).
[34] D. Jacquemart, C. Boursier, H. Elandaloussi, P. Jeseck, Y. Té, C. Janssen, J. Quant. Spectrosc. Radiat. Transfer (2021). HITRAN special issue.
[35] G. Toon, J.-F. Blavier, R. Washenfelder, D. Wunch, G. Keppel-Aleks, P. Wennberg, B. Connor, V. Sherlock, D. Griffith, N. Deutscher, J. Notholt, in: Advances in Imaging, Optical Society of America, 2009, p. JMA3.
[36] Y. Té, P. Jeseck, S. Payan, I. Pepin, C. Camy-Peyret, Rev. Sci. Instr. 81 (2010) 103102.
[37] C. Janssen, D. Simone, M. Guinet, Rev. Sci. Instr. 82 (2011) 034102–1–034102–10.
[38] W.-J. Ting, C.-H. Chang, S.-E. Chen, H.-C. Chen, J.-T. Shy, B. J. Drouin, A. M. Daly, J. Opt. Soc. Am. B 31 (2014) 1954–63.
[39] B. AlSaif, M. Lamperti, D. Gatti, P. Laporta, M. Fermann, A. Farooq, O. Lyulin, A. Campargue, M. Marangoni, J. Quant. Spectrosc. Radiat. Transfer 211 (2018) 172–8.
[40] A. G. Maki, J. S. Wells, 1998, Wavenumber calibration tables from heterodyne frequency measurements (version 1.3).
[41] V. Werwein, J. Brunzendorf, A. Serdyukov, O. Werhahn, V. Ebert, J. Mol. Spectrosc. 323 (2016) 28–42.
[42] V. Dana, J. Y. Mandin, A. Hamdouni, Appl. Opt. 31 (1992) 1937–41.
[43] H. Elandaloussi, C. Rouillé, P. Marie-Jeanne, C. Janssen, Appl. Opt. 55 (2016) 1971–7.
[44] C. Janssen, H. Elandaloussi, J. Gröbner, Atm. Meas. Tech. 11 (2018) 1707–23.
[45] A. G. Reule, J. Res. Natl. Inst. Stan. 80A (1976) 609–24.
[46] J. Birch, F. Clarke, Anal. Chim. Acta 380 (1999) 369–78.
[47] A. Feldman, D. Horowitz, R. M. Waxler, M. J. Dodge, Optical Materials Characterization, Technical Report Tech. Note. 993, Nat. Bur. Stand. (U.S.), 1978.
[48] H. H. Li, J. Phys. Chem. Ref. Data 5 (1976) 329.
[49] H. H. Li, J. Phys. Chem. Ref. Data 9 (1980) 161.
[50] M. Schilling, J. Stohner, Appl. Opt. 56 (2017) 4076–84.
[51] T. J. Johnson, R. L. Sams, T. A. Blake, S. W. Sharpe, P. M. Chu, Appl. Opt. 41 (2002) 2831–9.
[52] J. A. Kaye, J. Geophys. Res. 91 (1986) 7865–74.
[53] B. E. Poling, J. M. Prausnitz, J. P. O'Connel, The properties of gases and liquids, 5th ed., McGraw-Hill, 2001.
[54] C. Cobos, E. Castellano, H. J. Schumacher, J. Photochem. 21 (1983) 291–312.
[55] H. A. J. Meijer, W. J. Li, Isotopes Environ. Health Stud. 34 (1998) 349–69.
[56] D. Krankowsky, F. Bartecki, G. G. Klees, K. Mauersberger, K. Schellenbach, J. Stehr, Geophys. Res. Lett. 22 (1995) 1713–6.
[57] F. Bartecki, Mass spectroscometer investigations of ground air ozone isotopic composition, diploma thesis, University of Heidelberg, 1995. In German.
[58] J. Wen, M. H. Thiemens, J. Geophys. Res. 96 (1991) 10911–21.
[59] J. C. Johnston, M. H. Thiemens, J. Geophys. Res. 102 (1997) 25395–404.
[60] J. C. Johnston, Isotopic studies of tropospheric ozone, ph.d. thesis, University of California, San Diego, 1996.
[61] S. K. Bhattacharya, J. Savarino, B. Luz, Anal. Chem. 81 (2009) 5226–32.
[62] S. Mahata, S. K. Bhattacharya, C.-H. Wang, M.-C. Liang, Anal. Chem. 85 (2013) 6894–901. PMID: 23758535.
[63] S. Chakraborty, S. K. Bhattacharya, J. Chem. Phys. 118 (2003) 2164–72.
[64] J. E. Heidenreich, M. H. Thiemens, J. Chem. Phys. 78 (1983) 892–5.
[65] A. H. Laskar, R. Peethambaran, G. A. Adnew, T. Röckmann, Rapid Comm. Mass Spectrom. 33 (2019) 981–94.
[66] A. Pack, R. Tanaka, M. Hering, S. Sengupta, S. Peters, E. Nakamura, Rapid Comm. Mass Spectrom. 30 (2016) 1495–504.
[67] K. Prasanna, S. K. Bhattacharya, P. Ghosh, S. Mahata, M.-C. Liang, RSC Adv. 6 (2016) 51296–303.
[68] M. Dole, G. A. Lane, D. P. Rudd, D. A. Zaukelies, Geochim. Cosmochim. Acta 6 (1954) 65–78.
[69] E. Barkan, B. Luz, Rapid Comm. Mass Spectrom. 19 (2005) 3737–42.
[70] K. Mauersberger, B. Erbacher, D. Krankowsky, J. Günther, R. Nickel, Science 283 (1999) 370–2.
[71] C. Janssen, J. Guenther, D. Krankowsky, K. Mauersberger, J. Chem. Phys. 111 (1999) 7179–82.
[72] C. Janssen, J. Guenther, K. Mauersberger, D. Krankowsky, Phys. Chem. Chem. Phys. 3 (2001) 4718–21.
[73] D. Krankowsky, K. Mauersberger, Science 274 (1996) 1324–5.
[74] C. Janssen, B. Tuzson, J. Phys. Chem. A 114 (2010) 9709–19.
[75] J. Morton, J. Barnes, B. Schueler, K. Mauersberger, J. Geophys. Res. 95 (1990) 901–7.
[76] D. Krankowsky, P. Lämmerzahl, K. Mauersberger, C. Janssen, B. Tuzson, T. Röckmann, J. Geophys. Res. 112 (2007) D08301.
[77] M. Früchtl, C. Janssen, D. Taraborrelli, S. Gromov, T. Röckmann, Geophys. Res. Lett. 42 (2015) 8711–8.
[78] W. G. Mook, Environmental isotopes in the hydrological cycle: principles and applications, volume 1, International Atomic Energy Agency and United Nations Educational, Scientific and Cultural Organization, 2000.
[79] S. W. Sharpe, T. J. Johnson, R. L. Sams, P. M. Chu, G. C. Rhoderick, P. A. Johnson, Appl. Spectrosc. 58 (2004) 1452–61.
[80] E. Flores, J. Viallon, P. Moussay, R. I. Wielgosz, Appl. Spectrosc. 67 (2013) 1171–8.
[81] J. Ballard, R. J. Knight, D. Newnham, J. Vander Auwera, M. Herman, G. Di Lonardo, G. Masciarelli, F. M. Nicolaisen, J. A. Beukes, L. K. Christensen, R. McPheat, G. Duxbury, R. Freckleton, K. P. Shine, J. Quant. Spectrosc. Radiat. Transfer 66 (2000) 109 –28.
[82] D. B. Chase, Appl. Spectrosc. 38 (1984) 491–4.
[83] E. Theocharous, J. Ishii, N. P. Fox, Appl. Opt. 43 (2004) 4182–8.
[84] A. Kleinert, Appl. Opt. 45 (2006) 425–31.
[85] A. Keens, A. Simon, Correction of non-linearities in detectors in Fourier transform spectroscopy, US Patent #4,927,269, 1990.
[86] P. Jeseck, C. Camy-Peyret, S. Payan, T. Hawat, Appl. Opt. 37 (1998) 6544–9.
[87] G. P. Eppeldauer, A. L. Migdall, L. M. Hanssen, Metrologia 35 (1998) 485–90.
[88] L.-P. Boivin, Appl. Opt. 37 (1998) 1924–9.
[89] F. Bartoli, R. Allen, L. Esterowitz, M. Kruer, J. Appl. Phys. 45 (1974) 2150–4.
[90] M. C. Abrams, G. C. Toon, R. A. Schindler, Appl. Opt. 33

(1994) 6307–14.
[91] R. L. Richardson, H. Yang, P. R. Griffiths, Appl. Spectrosc. 52 (1998) 565–71.
[92] L. Shao, P. R. Griffiths, Anal. Chem. 80 (2008) 5219–24.
[93] J. Ballard, J. Remedios, H. K. Roscoe, J. Quant. Spectrosc. Radiat. Transfer 48 (1992) 733–41.
[94] J. W. C. Johns, Z. Lu, M. Weber, J. M. Sirota, D. C. Reuter, J. Mol. Spectrosc. (1996) 203–10.
[95] T. F. Deutsch, J. Phys. Chem. Solids 34 (1973) 2091–104.
[96] M. E. Thomas, W. J. Tropf, Handbook of optical constants of solids. 3. Elsevier Science; 1998, pp. 683–99.
[97] I. H. Malitson, J. Opt. Soc. Am. 54 (1964) 628–32.
[98] M. Birk, D. Hausamann, G. Wagner, J. W. Johns, Appl. Opt. 35 (1996) 2971–85.
[99] O. M. Lyulin, Atmos. Ocean. Opt. 28 (2015) 487–95.
[100] L. S. Rothman, C. P. Rinsland, A. Goldman, S. T. Massie, D. P. Edwards, J. M. Flaud, A. Perrin, C. Camy-Peyret, V. Dana, J. Y. Mandin, J. Schroeder, A. McCann, R. R. Gamache, R. B. Wattson, K. Yoshino, K. V. Chance, K. W. Jucks, L. R. Brown, V. Nemtchinov, P. Varanasi, J. Quant. Spectrosc. Radiat. Trans. 60 (1998) 665–710.
[101] F. Hase, T. Blumenstock, C. Paton-Walsh, Appl. Opt. 38 (1999) 3417–22.
[102] R. R. Gamache, E. Arie, C. Boursier, J. M. Hartmann, Spectrochim. Acta A 54 (1998) 35–63.
[103] L. Daneshvar, T. Földes, J. Buldyreva, J. Vander Auwera, J. Quant. Spectrosc. Radiat. Transfer 149 (2014) 258–74.
[104] R. R. Gamache, C. Roller, E. Lopes, I. E. Gordon, L. S. Rothman, O. L. Polyansky, N. F. Zobov, A. A. Kyuberis, J. Tennyson, S. N. Yurchenko, A. G. Császár, T. Furtenbacher, X. Huang, D. W. Schwenke, T. J. Lee, B. J. Drouin, S. A. Tashkun, V. I. Perevalov, R. V. Kochanov, J. Quant. Spectrosc. Radiat. Transf. 203 (2017) 70–87.
[105] Y. L. Babikov, S. N. Mikhailenko, A. Barbe, V. G. Tyuterev, J. Quant. Spectrosc. Radiat. Trans. 145 (2014) 169–96.
[106] T. B. Coplen, Pure Appl. Chem. 66 (1994) 273–6.
[107] P. Baertschi, Earth Planet. Sci. Lett. 31 (1976) 341–4.
[108] W. J. Li, B. L. Ni, D. Q. Jin, Q. G. Zhang, Kexue Tongbao 33 (1988) 1610–3.